ARTICLE IN PRESS

Available online at www.sciencedirect.com

ScienceDirect

Advances in Space Research xxx (xxxx) xxx

ADVANCES IN SPACE RESEARCH (a COSPAR publication)

www.elsevier.com/locate/asr

Spacecraft attitude estimation under attitude tracking maneuver during close-proximity operations

Daero Lee *, Sergio Gallucci

Scout Inc., Alexandria, VA, USA

Received 19 October 2022; received in revised form 15 December 2022; accepted 2 January 2023

Abstract

This paper presents a real-time relative three-axis attitude estimation using a camera and two gyros under momentum changes during close-proximity operations. The camera sensor provides quaternion measurements that relate the body frame of the deputy spacecraft with respect to the body frame of the chief spacecraft. The quaternion measurements are coupled with gyro measurements and attitude dynamics model in a multiplicative extended Kalman filter to determine relative attitude and gyro biases under momentum changes. The relative quaternion kinematics is augmented with spacecraft relative motion dynamics to represent the filter process dynamics. The quaternion measurements from a camera sensor and inertial measurement units (IMU) are utilized to the filter measurement model. The fault-tolerant attitude controller actuated by four reaction wheels, which has no unwinding problem is used for attitude tracking maneuvers during close-proximity operations in the presence of external disturbances, uncertain inertia parameter and actuator faults. This controller is combined with the extended Kalman filter to filter noisy measurements and to estimate gyro biases, which leads to a full-state feedback control system. Numerical simulations are performed to verify the effectiveness of the attitude estimation and control systems of the spacecraft with four reaction wheels during close-proximity operations of spacecraft in low-Earth orbit.

Keywords: Relative attitude estimation; Multiplicative extended Kalman filter; Fault-tolerant finite-time attitude control; Camera sensor; Quaternion measurements

1. Introduction

Precise attitude estimation is an essential technology for many space missions, such as close-proximity operations and docking with other spacecrafts, removal of large space debris objects, and reorientation of satellites (Jiang et al., 2016; Hu et al., 2017). This is a particularly interesting problem in spacecraft attitude dynamics since momentum change occurs. Particularly, an attitude maneuvering during close-proximity operations and docking may be be accomplished in the presence of external disturbances, parameter uncertainties, actuator system failures/faults, and even control input saturation. From a practical point of view, high-precision attitude estimation under the above conditions is an interesting and challenging problem. Sensors and actuators in spacecraft attitude control systems, including are critical subsystems and any fault of them can result in serious problems. In addition, unknown external disturbance and parameter uncertainty can increase the control tracking error and require more control effort. For these problems, an observer can be efficiently utilized to cope with any fault during control uses. Therefore, a fault-tolerant finite time controller (Jiang et al., 2016; Du et al., 2011; Zou, 2014) combined with a high-precision attitude estimation filter may be required to maintain high

* Corresponding author.
E-mail addresses: leed61@naver.com (D. Lee), sergio@scout.space (S. Gallucci).

https://doi.org/10.1016/j.asr.2023.01.004
0273-1177/

Please cite this article as: D. Lee and S. Gallucci, Spacecraft attitude estimation under attitude tracking maneuver during close-proximity operations, Advances in Space Research, https://doi.org/10.1016/j.asr.2023.01.004

reliability in the advanced control system design of spacecraft, accounting for possible control faults.

For spacecraft attitude tracking control problem, finite-time control is more desirable than asymptotic control in terms of faster convergence rate, higher precision control performance, and better disturbance rejection property (Jiang et al., 2016; Zou, 2014; Du et al., 2011; Lu and Xia, 2013; Shen et al., 2015). In Hu et al. (2017), Lu et al. (2016), Hu et al. (2013), a finite-time fault-tolerant control scheme was presented to address the spacecraft attitude stabilization problem under actuator faults, external disturbances, input saturation, and even inertia uncertainty simultaneously. In Zou (2014), a finite-time output feedback attitude tracking control law was proposed for rigid spacecraft based on the finite-time observer and continuous finite-time control techniques. In Xiao and Hu (2013), a compensation scheme withe finite-time convergence for reaction wheel faults and external disturbance was proposed for rigid spacecraft attitude tracking systems. Lan et al. (2017) addressed, the problem of finite-time disturbance observer (FTDO) design and the problem of FTDO-based finite-time control for system in a combined control approach. Cao et al. (2022) investigated a learning observer-based fault-tolerant control strategy for a rigid spacecraft attitude system with external disturbance, parameter uncertainty and actuator faults. The adaptive learning observer design approach does not require the upper bound information of generalized perturbation and estimates the attitude angular velocities and reconstruct actuator faults accurately and quickly. Sajjadi et al. (2021) proposed a nonlinear observer for high-speed estimation of the sample surface topography in a small duration of the probe transient motion utilizing a 2DOF model of TR-AFM. The proposed nonlinear observer can estimate the surface topography throughout transient oscillation of the microcantilever. Wang et al. (2022) an adaptive neuro-fuzzy integrated system (ANFIS) for satellite attitude estimation and control. The ANFIS system was proposed that can jointly control and estimate the system attitude. Pukdeboon and Siricharuanun (2014) developed a combined control which combines a FTDO and nonsingular terminal sliding mode (NTSM) technique for attitude tracking problem of rigid spacecraft. Tiwari et al. (2018) proposed spacecraft anti-unwinding attitude control using second-order sliding mode and robust adaptive non-singular fast terminal sliding mode control (NFTSM) method to commonly handle unwinding problem.

Most of the spacecraft use attitude sensors such as gyroscopes, camera sensors, star sensors, sun sensors and horizon sensors. Among these sensors, star sensors are known as the most precise, providing arc-second attitude accuracy (Liebe, 1995). For high precision attitude estimation of spacecraft, the combination of gyroscopes and star sensors are widely used because of their high precision. In this paper, a camera sensor is used for relative attitude estimation during close-proximity operations. Unlike other attitude sensors, camera sensors can be used for very close separation distance within several hundred meters between two spacecraft with high precision like star sensor performance. The relative sensor measurements used in this paper are quaternion measurements between two spacecraft. Quaternion measurements describing the relative attitude between the chief and deputy spacecraft are obtained from a camera-based attitude determination system. For real-time spacecraft attitude estimation an extended Kalman filter (EKF) algorithm has been widely used in nonlinear estimation problems (Schmidt, 1981; Lefferts et al., 1982). To represent attitude in the filter, several parameterizations are used such as Euler angles, quaternions, modified Rodrigues parameters and the rotation matrix. Quaternions are particularly attractive because they are non-singular, and bilinear in the kinematics equation (Kim et al., 2007; Crassidis and Junkins, 2008). However, the quaternion has a normalization constraint to obey, which can be violated by the linear measurement updates associated with the standard EKF approach (Lefferts et al., 1982; Kim et al., 2007; Crassidis and Junkins, 2008). To overcome this disadvantage, the multiplicative EKF (MEKF) was created using a multiplicative quaternion formulation where a three-component error vector is replaced with four-component quaternion (Lefferts et al., 1982; Kim et al., 2007). In Ref. Kim et al. (2007), Crassidis and Junkins (2008), the quaternion is represented by a three-dimensional vector of generalized Rodrigues parameters, such that the singularity can be placed anywhere from 180° to 360° and the normalization constraint of the quaternion is maintained in the update using quaternion multiplication. Abdelrahman and Park (2011) developed a spacecraft three-axis attitude and rate estimation algorithm based on magnetometer measurements and their time derivatives. The structure of the filter is built using spacecraft nonlinear dynamics in the presence of momentum exchange devices.

This paper presents a real-time relative attitude estimation using a camera sensor and two gyros under momentum changes by attitude tracking maneuvers during close-proximity operations. For relative spacecraft attitude estimation, a multiplicative extended Kalman filter (MEKF) is formulated to estimate the relative attitude and gyroscope biases of two spacecraft using quaternion measurements of a camera coupled with gyros measurements from each spacecraft during close-proximity operations. The angular velocity changes of the deputy spacecraft when momentum changes occur in close-proximity operations are measured by the gyro of the deputy spacecraft. The attitude state is the relative quaternion and gyro biases of the chief and deputy spacecraft. Inspired by the benefits of the proposed attitude estimation system and finite-time fault-tolerant control for spacecraft attitude tracking maneuvers, we propose an attitude determination and control system (ADCS) by combining the proposed attitude estimation system with the finite-time fault-tolerant attitude tracking of spacecraft control without unwinding in the presence of external disturbances, uncertain inertia parameter, actuator faults, and input saturation in Refs. Lee and Leeghim (2020), Lee

(2021). However, the finite-time fault-tolerant controls (Lee and Leeghim, 2020; Lee, 2021) do not use the attitude state estimation and show attitude tracking control. The proposed ADCS system was developed to use for high-precision relative attitude estimation and finite-time attitude tracking maneuvers of the deputy spacecraft with four reaction wheels during close-proximity operations. For this goal, the proposed MEKF is combined with the composite finite-time fault-tolerant controller of the deputy spacecraft with four reaction wheels (Lee and Leeghim, 2020) to provide the state estimates, which can be used in place of the "true" states. The controller clearly requires full-state knowledge, which is not always possible or even practical in real-world systems. The required full-state knowledge is the relative quaternion and relative angular velocity. Unlike the relative quaternion, the relative angular velocity of two spacecraft is computed using the estimated state. The used controller for a proposed ADCS is a composite controller which consists of a non-singular fast terminal sliding mode control (NFTSMC) scheme combined with a feed-forward term based on finite-time disturbance observer (FTDO) technique. The controller has no the singularity and unwinding problem. The global final stability of the attitude tracking control system is achieved in the presence of external disturbances, inertia uncertainty, and actuator faults.

Thus, the contribution of this study can be summarized. First, a high-precision relative attitude estimation system using quaternion measurements from a camera sensor and two gyros of the chief and deputy spacecraft was developed for relative attitude estimation during close-proximity maneuvers/operations. Second, the ADCS was proposed by the full-state feedback form where the FTDO-based NFTSMC is combined with the developed relative attitude estimation system to provide a full-state knowledge. The ADCS system has finite-time stability and anti-unwinding capability in the presence of external disturbances, inertia uncertainty, and actuator faults. Compared to the previous studies (Lee and Leeghim, 2020; Lee, 2021), this study shows attitude tracking control maneuver with full-state feedback by combining with the high-precision attitude estimation system to produce more reliable attitude tracking maneuver. Furthermore, this study shows that the relative attitude estimation can can performed while the control moment using tetrahedron configuration of reaction wheels is used. Third, the effectiveness of the proposed relative attitude estimation system and the ADCS system are verified with numerical simulations for an attitude tracking control maneuver during close-proximity operations.

2. Relative attitude kinematics and dynamics

2.1. Quaternion kinematics

In this section, relative quaternion kinematics is briefly reviewed. The relative quaternion $\boldsymbol{q}$, which maps from vectors in the chief frame to the vectors in the deputy frame, is given by

$$\boldsymbol{q} = \boldsymbol{q}_d \otimes \boldsymbol{q}_c^{-1}, \tag{1}$$

where $\boldsymbol{q}_c$ and $\boldsymbol{q}_d$ are the attitudes of the chief and deputy spacecraft, respectively, relative to an inertial frame. The quaternion is defined by $\boldsymbol{q} \equiv [\boldsymbol{\varrho} q_4]^T$, with $\boldsymbol{\varrho} \equiv [q_1 q_2 q_3]^T = \boldsymbol{e}\sin(\vartheta)$ and $q_4 = \cos(\vartheta/2)$, where $\boldsymbol{e}$ is the axis of rotation and ϑ is the angle of rotation (Lefferts et al., 1982). The quaternion possesses three degrees of freedom and satisfies the constraint $\|\boldsymbol{q}\| = 1$. The attitude matrix related to the quaternion is given by

$$A(\boldsymbol{q}) = \left(q_4^2 - \|\boldsymbol{\varrho}\|\right) + 2\boldsymbol{\varrho}\boldsymbol{\varrho} - 2q_4\boldsymbol{\varrho}^\times = \Xi^T(\boldsymbol{q})\Psi(\boldsymbol{q}) \tag{2}$$

with

$$\Xi(\boldsymbol{q}) = \begin{bmatrix} q_4 I_{3\times3} + \boldsymbol{\varrho}^\times \\ -\boldsymbol{\varrho}^T \end{bmatrix}, \quad \Psi(\boldsymbol{q}) = \begin{bmatrix} q_4 I_{3\times3} - \boldsymbol{\varrho}^\times \\ -\boldsymbol{\varrho}^T \end{bmatrix}, \tag{3}$$

where $I_{3\times3}$ is an identity matrix and $\boldsymbol{\varrho}^\times$ is a cross product matrix defined by

$$\boldsymbol{\varrho}^\times = \begin{bmatrix} 0 & -q_3 & q_2 \\ q_3 & 0 & -q_1 \\ -q_2 & q_1 & 0 \end{bmatrix}. \tag{4}$$

In this paper, quaternion multiplication is defined using the convention of Lefferts et al. (1982) where quaternion multiplication expression appears in the same order as the attitude matrix multiplication: $A(\boldsymbol{q}')A(\boldsymbol{q}) = A(\boldsymbol{q}' \otimes \boldsymbol{q})$.

$$A(\boldsymbol{q}\prime)A(\boldsymbol{q}) = A(\boldsymbol{q}\prime \otimes \boldsymbol{q}) = [\,\Psi(\boldsymbol{q}') \quad \boldsymbol{q}'\,]\boldsymbol{q} = [\,\Xi(\boldsymbol{q}) \ \boldsymbol{q}\,]\boldsymbol{q}'. \tag{5}$$

The inverse of the quaternions is given by

$$\boldsymbol{q}^{-1} = \left[-\boldsymbol{\varrho}^T \ q_4\right]^T. \tag{6}$$

Note that this quaternion product $\boldsymbol{q} \otimes \boldsymbol{q}^{-1} = [0001]^T$, which is the identity quaternion. The quaternion kinematic is given by

$$\dot{\boldsymbol{q}} = \frac{1}{2}\Xi(\boldsymbol{q})\boldsymbol{\omega}_e, \tag{7}$$

where $\boldsymbol{\omega}_e$ is the relative angular velocity of the deputy spacecraft relative to the chief spacecraft in the deputy's body-fixed frame. The relative angular velocity $\boldsymbol{\omega}_e$ in (7) is defined by

$$\boldsymbol{\omega}_e = \boldsymbol{\omega}_d - A(\boldsymbol{q})\boldsymbol{\omega}_c, \tag{8}$$

where $\boldsymbol{\omega}_c$ and $\boldsymbol{\omega}_d$ are the angular velocities of the chief and deputy spacecraft in their body-fixed frames, respectively. A discrete-time propagation of the relative quaternion kinematics Eq. (7), assuming that $\boldsymbol{\omega}_c$ and $\boldsymbol{\omega}_d$ are constant over the sampling interval $\Delta t \approx t_{k+1} - t_k$, is given by Mayo (1978)

$$\hat{\boldsymbol{q}}_{k+1} = \overline{\Omega}(\boldsymbol{\omega}_{d_k})\overline{\Gamma}(\boldsymbol{\omega}_{c_k})\hat{\boldsymbol{q}}_k, \tag{9}$$

with

$$\overline{\Omega}(\boldsymbol{\omega}_{d_k}) = \begin{bmatrix} \cos\left(\frac{1}{2}\|\boldsymbol{\omega}_{d_k}\|\Delta t\right) I_{3\times 3} - \left(\hat{\psi}_k^+\right)^\times & \boldsymbol{\psi}_k \\ -\boldsymbol{\psi}_k^T & \cos\left(0.5\|\boldsymbol{\omega}_{d_k}\|\Delta t\right) \end{bmatrix} \tag{10a}$$

$$\overline{\Gamma}(\boldsymbol{\omega}_{c_k}) = \begin{bmatrix} \cos\left(\frac{1}{2}\|\boldsymbol{\omega}_{c_k}\|\Delta t\right) I_{3\times 3} - [\zeta_k]^\times & -\zeta_k \\ -\zeta_k^T & \cos\left(\frac{1}{2}\|\boldsymbol{\omega}_{c_k}\|\Delta t\right) \end{bmatrix} \tag{10b}$$

where

$$\boldsymbol{\psi}_k = \frac{\sin\left(\frac{1}{2}\|\boldsymbol{\omega}_{d_k}\|\Delta t\right)\boldsymbol{\omega}_{d_k}}{\|\boldsymbol{\omega}_{d_k}\|},\ \boldsymbol{\zeta}_k = \frac{\sin\left(\frac{1}{2}\|\boldsymbol{\omega}_{c_k}\|\Delta t\right)\boldsymbol{\omega}_{c_k}}{\|\boldsymbol{\omega}_{c_k}\|}. \tag{11}$$

2.2. Relative attitude dynamics

To achieve attitude control with high performance, redundant actuators are usually mounted on the spacecraft (Hu et al., 2017; Hu et al., 2013). In this paper, the actuators with redundancy ($m > 3$) are considered for the attitude control system design of the deputy spacecraft.

$$J\dot{\boldsymbol{\omega}}_d = -\boldsymbol{\omega}_d^\times J\boldsymbol{\omega}_d + D\boldsymbol{u} + \boldsymbol{d}_0, \tag{12}$$

where $D \in \mathbb{R}^{3\times m}$ is the actuator configuration matrix, $\boldsymbol{u} = [u_1 u_2 \cdots u_m]^T \in \mathbb{R}^m$ denotes the applied control torque on the spacecraft produced by m actuators, and $\boldsymbol{d}_0$ represents all external disturbances experienced by the spacecraft. The matrix $J \in \mathbb{R}^{3\times 3}$ denotes the positive-definite inertia matrix of the spacecraft composed of both nominal component J_0 and uncertain term ΔJ and is described as $J = J_0 + \Delta J$.

To handle actuator fault problems, the applied control in (12) includes the uniform actuator fault model described for all possible modes (Hu et al., 2013; Lee and Leeghim, 2020).

$$\boldsymbol{u} = \boldsymbol{u}_c + E(\overline{\boldsymbol{u}} - \boldsymbol{u}_c), \tag{13a}$$

$$u_i = u_{c_i} + E_i(\overline{u}_i - u_{c_i}), \quad i = 1, 2, \cdots, m, \tag{13b}$$

where $\boldsymbol{u}_c = [u_{c_1}\ u_{c_2}\ \cdots\ u_{c_m}]^T \in \mathbb{R}^m$ is the commanded control by the controller and $E = \mathrm{diag}(E_1, E_2, \cdots, E_m) \in \mathbb{R}^{m\times m}$ is the actuator effectiveness matrix. E_i is the failure indicator for the i^{th} actuator, $\overline{u}_i$ represents uncertain stuck failures for the i^{th} actuator, and u_{c_i} is the i^{th} actuator's desired control commanded by the controller. Note that the case $E_i = 0$ means that the i^{th} actuator works normally. If $E_i = 1$, the i^{th} actuator fails completely without any control torque generated. $E_i \in (0, 1)$ corresponds to the case in which the i^{th} has partially lost its effectiveness, but it still works for all of the time. The presented fault model can represent outage, loss of effectiveness, and stuck faults. These three types of the actuator faults as summarized as in Table 1. Next, we consider the spacecraft dynamics with actuator faults by incorporating the deputy spacecraft dynamics (12) with the actuator fault model in the following form:

Table 1
Actuator fault model (Hu et al., 2013).

Fault model	$\overline{\boldsymbol{u}}_i$	E_i
Normal	0	0
Outage	0	1
Loss of effectiveness	0	$0 < E_i < 1$
Stuck	$\overline{u}_i$	1

$$J\dot{\boldsymbol{\omega}}_d = -\boldsymbol{\omega}_d^\times J\boldsymbol{\omega}_d + D((I - E)\boldsymbol{u}_c + E\overline{\boldsymbol{u}}) + \boldsymbol{d}_0. \tag{14}$$

Suppose that the chief spacecraft quaternion, $\boldsymbol{q}_c$, is given that also follows the following kinematics equation:

$$\dot{\boldsymbol{q}}_c = Q(\boldsymbol{q}_c)\omega_c, \tag{15}$$

where $\boldsymbol{\omega}_c \in \mathbb{R}^3$ is the angular velocity vector of the chief spacecraft. In this study, the attitude dynamics of the chief is assumed to follow the torque-free rotation of spacecraft (Tewari, 2007) where the external torque is zero.

$$J_c\dot{\boldsymbol{\omega}}_c + \boldsymbol{\omega}_c^\times J_c\boldsymbol{\omega}_c = \boldsymbol{0}. \tag{16}$$

In a similar manner the relative dynamics with actuator fault is defined in Hu et al. (2013), Lee (2017) as

$$\begin{aligned} J\dot{\boldsymbol{\omega}}_e = &-(\boldsymbol{\omega}_e + A(\boldsymbol{q})\boldsymbol{\omega}_c)^\times J(\boldsymbol{\omega}_e + A(\boldsymbol{q})\boldsymbol{\omega}_c) \\ &+ J\left(\boldsymbol{\omega}_e^\times A(\boldsymbol{q})\boldsymbol{\omega}_c + A(\boldsymbol{q})J_c^{-1}\boldsymbol{\omega}_c^\times J_c\boldsymbol{\omega}_c\right) \\ &+ D(I - E)\boldsymbol{u}_c + DE\overline{\boldsymbol{u}} + \boldsymbol{d}_0. \end{aligned} \tag{17}$$

Since the inverse of inertia matrix, J^{-1} is given by Lee (2017)

$$\begin{aligned} J^{-1} &= (J_0 + \Delta J_0)^{-1} = (J_0)^{-1} - \left(J_0 + J_0\Delta J^{-1}J_0\right)^{-1} \\ &= J_0^{-1} + \Delta\tilde{J}, \end{aligned} \tag{18}$$

Multiplying both sides of (17) by (18) and arranging about J_0, the relative attitude dynamics (17) is described as

$$\begin{aligned} \dot{\boldsymbol{\omega}}_e = &-J_0^{-1}(\boldsymbol{\omega}_e + A(\boldsymbol{q})\boldsymbol{\omega}_c)^\times J_0(\boldsymbol{\omega}_e + A(\boldsymbol{q})\boldsymbol{\omega}_c) \\ &+ \left(\boldsymbol{\omega}_e^\times A(\boldsymbol{q})\boldsymbol{\omega}_c + A(\boldsymbol{q})J_c^{-1}\boldsymbol{\omega}_c^\times J_c\boldsymbol{\omega}_c\right) + J_0^{-1}\boldsymbol{u}_c^\star \\ &+ J_0^{-1}\boldsymbol{d}, \end{aligned} \tag{19}$$

where $\boldsymbol{u}_c^\star = D\boldsymbol{u}_c$ is the control command by the controller. The rotational dynamics of the deputy relative to the chief is then described in the body-fixed frame of the deputy spacecraft.

$$\begin{aligned} \boldsymbol{d} = \Big[&\boldsymbol{d}_0 + DE(-\boldsymbol{u}_c + \overline{\boldsymbol{u}}) - J_0\Delta\tilde{J}\left((\boldsymbol{\omega}_e + A(\boldsymbol{q})\boldsymbol{\omega}_c)^\times J(\boldsymbol{\omega}_e + A(\boldsymbol{q})\boldsymbol{\omega}_c)\right) \\ &-(\boldsymbol{\omega}_e + A(\boldsymbol{q})\boldsymbol{\omega}_c)^\times \Delta J(\boldsymbol{\omega}_e + A(\boldsymbol{q})\boldsymbol{\omega}_c) + J_0\Delta\tilde{J}(D(I - E)\boldsymbol{u}_c + DE\overline{\boldsymbol{u}})\Big], \end{aligned} \tag{20}$$

The left side of Eq. (20) $\boldsymbol{d}$ is the lumped disturbance including actuator faults, uncertain inertia matrix and unknown external disturbances. The lumped disturbance $\boldsymbol{d}$ in (20) is bounded, but its bound limit is not known in advance.

The adopted finite-time observer provides the estimate of the lumped disturbance, $\boldsymbol{d}$.

3. Sensor models

3.1. Camera measurement model

In this study, a camera sensor provides quaternion measurements that relate the attitude of the deputy frame with respect to the chief frame is used. The output of a camera sensor is an estimated quaternion that relates the relative orientation of the body frames of two spacecraft. The camera sensor frame coincides with the body-fixed frame of the spacecraft. The quaternion measurements are assumed to be unbiased, but they have added random measurement noise. To generate synthetic measurements the following model is used and the discrete-time quaternion measurement is then given by

$$\tilde{\boldsymbol{q}}_k = \begin{bmatrix} \frac{1}{2}\boldsymbol{v}_k \\ 1 \end{bmatrix} \otimes \boldsymbol{q}_k = \boldsymbol{q}_k + \frac{1}{2}\Xi(\boldsymbol{q}_k)\boldsymbol{v}_k, \qquad \text{(21a)}\tilde{\boldsymbol{q}}_k = \frac{\tilde{\boldsymbol{q}}_k}{\|\tilde{\boldsymbol{q}}_k\|}, \text{(21b)}$$

where $\tilde{\boldsymbol{q}}_k$ is the quaternion measurement with the quaternion normalization, $\boldsymbol{q}_k$ is the true quaternion of the spacecraft, and $\boldsymbol{v}_k \in \mathbb{R}^3$ is the zero mean Gaussian white noise with the characteristics of

$$E\left(\boldsymbol{v}_k\boldsymbol{v}_k^T\right) = \sigma_m^2 I_{3\times3}, \tag{22}$$

where σ_m is the standard deviation of a camera sensor measurement error. The matrix used to make up the MEKF measurements error covariance matrix is given by

$$R_k = \sigma_m^2 I_{3\times3}. \tag{23}$$

The measurement residual or innovation vector is defined using a multiplicative error quaternion in the body-fixed frame, given by

$$\delta\boldsymbol{q}_k = \tilde{\boldsymbol{q}}_k \otimes \hat{\boldsymbol{q}}_k^{-1}, \tag{24}$$

with $\delta\boldsymbol{q}_k = \left[\delta\boldsymbol{q}_{k_v}^T \, \delta q_{k_4}\right]^T$ and $\hat{\boldsymbol{q}}_k$ is the estimated quaternion at kth epoch.

3.2. Imaging model

The quaternion measurement is limited in resolution by a Gaussian error applied due to the functional resolution of the optical system. This resolution is defined with a combination of ground spatial distance (GSD) between the focal plane and any feature or resident space object of interest, and optical solution coefficients representing the predicted sensor response $\text{FWHM}_{PSF/LSF}$, validated experimentally, to yield a feature resolution as a function of distance. The feature resolution, $\text{Res} = \text{GSD} \times \text{FWHM}_{PSF/LSF}$ is a theoretical measurement that uses the sensor and optical elements' characteristics to define the size of a projected pixel from the focal plane upon the feature of interest. The focal length f_l is commonly defined in millimeters, pixel pitch p is the distance between pixels on the focal plane, and measured in micrometers, and the distance between the focal plane and feature of interest, D, is commonly measured in kilometers. The GSD is also given by

$$\text{GSD} = \frac{Dp}{f_l} \tag{25}$$

A single pixel is not enough to gather significant data upon an object, however, so the functional resolution of the optical system is modulated by its quality, Q. The Q of the system represents its detector sampling frequency, or optical band pass limit, and is calculated as below per the optical wavelength of the sensor, λ:

$$Q = \frac{\lambda f_l}{p} \tag{26}$$

The full width half maximum of a point spread function, or $\text{FWHM}_{PSF/LSF}$, is a measure of acutance of a sensor, and determines the minimum feature identifiable by the sensor. This feature can be identified by computer vision algorithms; assuming a Gaussian representation of the feature of interest and deviation discernible by perception from a viewer or algorithm, the Z-score can be used to determine whether any individual pixel on the focal plane will result in an identification of the feature of interest. This propagates across multiple pixels if the coherent pattern is visible. Therefore, a Z-score for the feature standard deviation from the feature of interest is used for a $\text{FWHM}_{PSF/LSF}$ calculation given by

$$\text{FWHM}_{PSF/LSF} = QZ \tag{27}$$

Therefore, the functional full sampling resolution of the spacecraft optical solution, measured in units of m^2 of resolution per m of distance between focal plane and feature of interest, is defined as:

$$\text{Res} = \text{GSD} \times \text{FWHM}_{PSF/LSF} \tag{28}$$

Fig. 1 shows the basis for an optical/camera sensor measurement of characteristic features, namely a geometric shape in space. The $\text{FWHM}_{PSF/LSF}$ is provided by the sensor response curve binned across discrete pixels on the sensor. The resolution of any sensor is limited by its size and pixel pitch, tied to the optical system's inherent quality for input resolved imagery. A convolutional neural network (Park et al., 2019) trained with synthetic representative scenarios is used to validate the simulation and vice versa in a loosely-coupled loop. A pipeline integrating simulated chief spacecraft attitude and the focal plane has been used to provide this efficacy function: the convolutional neural network is not capable of ideal determination of the attitude of the observed spacecraft, and therefore an efficacy function has been used to modulate simulation results to realistic and predictable ones, currently not accounting for adverse lighting conditions or false-negative identification rates.

$$\sigma_q = \tan^{-1}\left(\frac{\text{Res}}{2D}\right) \tag{29}$$

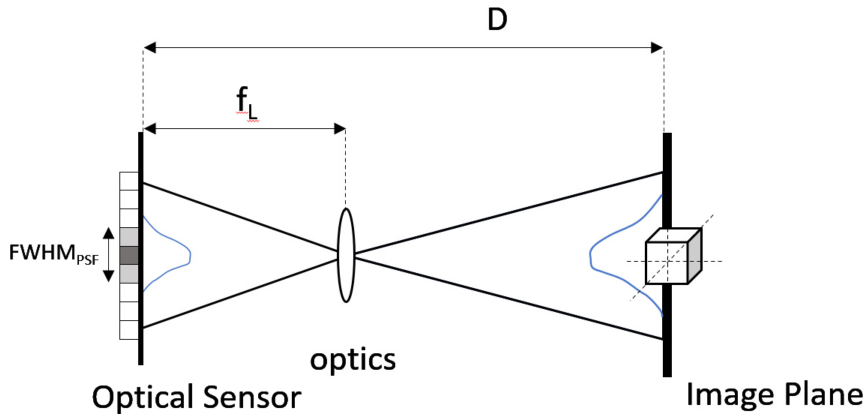

Fig. 1. A conceptual representation of an optical/camera sensor conducting imaging of a sample geometry.

The resolution limitation implies the fundamental Nyquist-sourced sampling error: this can be used for a Gaussian error assessment of the bearing attainable by the optical sensor. The output 3σ error is consequently used in this study for a uncertainty determination in state measurement.

3.3. Gyro measurement model

A rate integrating gyroscope which measures the angular velocity is used with a star tracker to improve the attitude estimation accuracy. For this sensor, a widely used measurement model is given by Farrenkopf (1978)

$$\tilde{\boldsymbol{\omega}}(t) = \boldsymbol{\omega}(t) + \boldsymbol{\beta}(t) + \boldsymbol{\eta}_v(t), \tag{30}$$

$$\dot{\boldsymbol{\beta}}(t) = \boldsymbol{\eta}_u(t). \tag{31}$$

where $\tilde{\boldsymbol{\omega}}(t)$ is the continuous-time measured angular rate, $\boldsymbol{\beta}$ is the time-varying gyro bias, $\boldsymbol{\eta}(t)_v$ and $\boldsymbol{\eta}(t)_u$ are independent zero-mean Gaussian white-noise process with

$$E\{\boldsymbol{\eta}_v(t)\boldsymbol{\eta}_v^T(\tau)\} = I_{3\times3}\sigma_v^2\delta(t-\tau) \tag{32a}$$

$$E\{\boldsymbol{\eta}_u(t)\boldsymbol{\eta}_u^T(\tau)\} = I_{3\times3}\sigma_u^2\delta(t-\tau) \tag{32b}$$

where $\delta(t-\tau)$ is the Dirac delta function. The parameters of the chief and deputy gyros are denoted by $(\boldsymbol{\eta}_{cv}, \boldsymbol{\eta}_{cu})$ and $(\boldsymbol{\eta}_{dv}, \boldsymbol{\eta}_{du})$, respectively. The discrete-time gyro measurements can be generated using the following recursive equations (Crassidis, 2005):

$$\tilde{\boldsymbol{\omega}}_{k+1} = \boldsymbol{\omega}_{k+1} + \frac{1}{2}(\boldsymbol{\beta}_{k+1} + \boldsymbol{\beta}_k) + \left(\frac{\sigma_v^2}{\Delta t} + \frac{1}{12}\sigma_u^2\Delta t\right)\boldsymbol{N}_{vk}, \tag{33}$$

$$\boldsymbol{\beta}_{k+1} = \boldsymbol{\beta}_k + \sigma_v\Delta t^{1/2}\boldsymbol{N}_{vk} \tag{34}$$

where the script k denotes the k^{th} time-step, Δt is the gyro sampling interval, and $\boldsymbol{N}_{vk}$ and $\boldsymbol{N}_{uk}$ are zero-mean Gaussian white-noise processes with spectral densities given by $\sigma_v^2 I_{3\times3}$ and $\sigma_u^2 I_{3\times3}$, respectively.

4. Relative attitude estimation

In this section, the MEKF implementation equations for relative spacecraft attitude estimation are shown. The relative quaternion and gyro biases for the chief and deputy spacecraft are estimated. The estimate equations are given by

$$\dot{\hat{\boldsymbol{q}}} = \frac{1}{2}\Xi(\hat{\boldsymbol{q}})\boldsymbol{\omega}_e, \tag{35a}$$

$$\hat{\boldsymbol{\omega}}_{dc} = \hat{\boldsymbol{\omega}}_e = \hat{\boldsymbol{\omega}}_d - A(\hat{\boldsymbol{q}})\hat{\boldsymbol{\omega}}_c, \tag{35b}$$

$$\dot{\hat{\boldsymbol{\beta}}}_c = \boldsymbol{0}, \tag{35c}$$

$$\dot{\hat{\boldsymbol{\beta}}}_d = \boldsymbol{0}, \tag{35d}$$

$$\hat{\boldsymbol{\omega}}_c = \tilde{\boldsymbol{\omega}}_d - \hat{\boldsymbol{\beta}}_c, \tag{35e}$$

$$\hat{\boldsymbol{\omega}}_d = \tilde{\boldsymbol{\omega}}_d - \hat{\boldsymbol{\beta}}_d. \tag{35f}$$

The error-state dynamics are now given by Kim et al. (2007)

$$\delta\dot{\boldsymbol{x}} = F\delta\boldsymbol{x} + G\boldsymbol{w}. \tag{36}$$

with

$$\delta\boldsymbol{x} = \left[\delta\boldsymbol{\alpha}^T\ \delta\boldsymbol{\beta}_c^T\ \delta\boldsymbol{\beta}_d^T\right]^T\ \boldsymbol{w} = \left[\boldsymbol{\eta}_{cv}^T\ \boldsymbol{\eta}_{dv}^T\ \boldsymbol{\eta}_{cu}^T\ \boldsymbol{\eta}_{du}^T\right]^T, \tag{37}$$

where

$$F = \begin{bmatrix} -\hat{\boldsymbol{\omega}}_d^{\times} & A(\hat{\boldsymbol{q}}) & -I_{3\times3} \\ 0_{3\times3} & 0_{3\times3} & 0_{3\times3} \\ 0_{3\times3} & 0_{3\times3} & 0_{3\times3} \end{bmatrix},$$
$$G = \begin{bmatrix} A(\hat{\boldsymbol{q}}) & -I_{3\times3} & 0_{3\times3} & 0_{3\times3} \\ 0_{3\times3} & 0_{3\times3} & 0_{3\times3} & 0_{3\times3} \\ 0_{3\times3} & 0_{3\times3} & 0_{3\times3} & 0_{3\times3} \end{bmatrix}. \tag{38}$$

and the spectral density matrix of the process noise $\boldsymbol{w}$ is given by

$$Q = \begin{bmatrix} \sigma_{cv}^2 I_{3\times3} & 0_{3\times3} & 0_{3\times3} & 0_{3\times3} \\ 0_{3\times3} & \sigma_{dv}^2 I_{3\times3} & 0_{3\times3} & 0_{3\times3} \\ 0_{3\times3} & 0_{3\times3} & \sigma_{cu}^2 I_{3\times3} & \sigma_{dv}^2 I_{3\times3} \end{bmatrix}. \tag{39}$$

Note that the F matrix is 9×9 matrix now, since the order of the system has been reduced from 10 state to 9 state. The linearization of the quaternion measurement is obtained using a multiplicative error quaternion between the quaternion measurement and the estimated quaternion, given by

$$\delta\hat{\boldsymbol{q}}_k^+ = \tilde{\boldsymbol{q}}_k \otimes \hat{\boldsymbol{q}}_k^{-1}, \tag{40}$$

with $\delta\boldsymbol{q} = \left[\delta\boldsymbol{\rho}_k \quad \delta q_{4_k}\right]$. Then the measurement residual $\tilde{\boldsymbol{y}}_k - \boldsymbol{h}_k(\hat{\boldsymbol{q}}_k^-)$ is replaced with $2\delta\boldsymbol{\rho}_k$. By the small angle approximation $\delta\boldsymbol{\rho} \approx \delta\boldsymbol{\alpha}/2$, where $\delta\boldsymbol{\alpha}$ has components of roll, pitch, and yaw angles for any rotation sequence. The factor of 2 is multiplied with the vector part of the error quaternion because the angle error is used in the MEKF. The measurement-state mapping matrix is therefore given by

$$H_k(\boldsymbol{x}_k^-) = [I_{3\times3}\ 0_{3\times3}\ 0_{3\times3}]. \tag{41}$$

and R_k is given by a 3×3 covariance matrix of the attitude errors. Note that the number of columns of $H_k(\boldsymbol{x}_k^-)$ is nine, which is the dimension of the reduced-order state.

The final part of the MEKF involves the quaternion and biases updates. The error-state update follows

$$\Delta\hat{\tilde{\boldsymbol{x}}}^+ = K_k\left[\tilde{\boldsymbol{y}}_k - \boldsymbol{h}_k(\hat{\boldsymbol{x}}_k^-)\right]. \tag{42}$$

where $\Delta\hat{\tilde{\boldsymbol{x}}}^+ = \left[\delta\hat{\boldsymbol{\alpha}}_k^{+T}\ \Delta\hat{\boldsymbol{\beta}}_{c_k}^{+T}\ \Delta\hat{\boldsymbol{\beta}}_{d_k}^{+T}\right]^T$, $\tilde{\boldsymbol{y}}_k$ is the measurement output, and $\boldsymbol{h}_k(\hat{\boldsymbol{x}}_k^-)$ is the estimated quaternion output, given by

$$\boldsymbol{h}_k(\hat{\boldsymbol{x}}_k^-) = \hat{\boldsymbol{q}}_k^- \tag{43}$$

The gyro bias updates of of the chief and deputy are simply given by

$$\hat{\boldsymbol{\beta}}_{c_k}^+ = \hat{\boldsymbol{\beta}}_{c_k}^- + \Delta\hat{\boldsymbol{\beta}}_{c_k}^+,\ \hat{\boldsymbol{\beta}}_{d_k}^+ = \hat{\boldsymbol{\beta}}_{d_k}^- + \Delta\hat{\boldsymbol{\beta}}_{d_k}^+. \tag{44}$$

The quaternion update is more complicated. As previously mentioned the fourth component of $\delta\boldsymbol{q}_k$ is nearly one. Therefore, to within first-order the quaternion update is computed using Eq. (5) and the quaternion multiplication of the rule of Eq. (40), given by

$$\hat{\boldsymbol{q}}_k^+ = \delta\hat{\boldsymbol{q}}_k^+ \otimes \hat{\boldsymbol{q}}_k^- = \begin{bmatrix} \frac{1}{2}\hat{\boldsymbol{\alpha}}_k^+ \\ 1 \end{bmatrix} \otimes \hat{\boldsymbol{q}}_k^- = \hat{\boldsymbol{q}}_k^- + \frac{1}{2}\Xi(\hat{\boldsymbol{q}}_k^-)\hat{\boldsymbol{\alpha}}_k^+. \tag{45}$$

This updated quaternion is a unit vector to within first-order; however, a brute-force normalization should be performed to insure $\hat{\boldsymbol{q}}_k^{+T}\hat{\boldsymbol{q}}_k^+ = 1$. In the standard EKF formulation, given a post-update estimates $\hat{\boldsymbol{\beta}}_{c_k}^+$ and $\hat{\boldsymbol{\beta}}_{d_k}^+$, the post-update angular velocities and propagated gyro bias of the chief and deputy follow

$$\hat{\boldsymbol{\omega}}_{c_k}^+ = \tilde{\boldsymbol{\omega}}_{c_k}^+ - \hat{\boldsymbol{\beta}}_k^+,\ \hat{\boldsymbol{\beta}}_{c_{k+1}}^- = \hat{\boldsymbol{\beta}}_{c_k}^+, \tag{46a}$$

$$\hat{\boldsymbol{\omega}}_{d_k}^+ = \tilde{\boldsymbol{\omega}}_{d_k}^+ - \hat{\boldsymbol{\beta}}_k^+,\ \hat{\boldsymbol{\beta}}_{d_{k+1}}^- = \hat{\boldsymbol{\beta}}_{d_k}^+. \tag{46b}$$

The attitude estimation algorithm is summarized in Table 2. The filter is first initialized with a known state (the bias initial condition is usually assumed zero) and error-covariance matrix. The first three diagonal elements of the error-covariance matrix correspond to attitude errors. Then, the Kalman gain is computed using the measurement-error covariance R_k and sensitivity matrix H_k in Eq. (41). The state error-covariance follows the standard EKF update, while the error-state update is computed using Eq. (45). The biases and quaternion updates are now given by Eqs. (44) and (45). Also, the updated quaternion is re-normalized by brute force. Finally, the estimated angular velocity is used to propagate the quaternion kinematics model in Eq. (35a) and standard error-covariance in the MEKF. Note that the gyro biases propagation is constant as shown by Eqs. (35c) and (35d).

Table 2
Multiplicative extended Kalman filter for relative attitude estimation.

Initialize	$\hat{\boldsymbol{q}}(t_0) = \hat{\boldsymbol{q}}_0,\ \hat{\boldsymbol{\beta}}_c(t_0) = \hat{\boldsymbol{\beta}}_{c_0},\ \hat{\boldsymbol{\beta}}_c(t_0) = \hat{\boldsymbol{\beta}}_{c_0},\ P(t_0) = P_0$
Gain	$K_k = P_k^- H_k^T\left[(\hat{\boldsymbol{q}}_k^-)P_k^- H_k^T((\hat{\boldsymbol{q}}_k^-)) + R_k\right]^-1$ $H_k(\hat{\boldsymbol{q}}_k^-) = [I_{3\times3}\ 0_{3\times3}\ 0_{3\times3}]$
Update	$H_k(\hat{\boldsymbol{q}}_k^-) = [I_{3\times3}\ 0_{3\times3}\ 0_{3\times3}]$ $\Delta\hat{\tilde{\boldsymbol{x}}}^+ = K_k[\tilde{\boldsymbol{y}}_k - \boldsymbol{h}_k(\hat{\boldsymbol{x}}_k^-)]$ $\Delta\hat{\tilde{\boldsymbol{x}}}^+ = \left[\delta\hat{\boldsymbol{\alpha}}_k^{+T}\ \Delta\hat{\boldsymbol{\beta}}_{c_k}^{+T}\ \Delta\hat{\boldsymbol{\beta}}_{d_k}^{+T}\right]^T$ $\boldsymbol{h}_k(\hat{\boldsymbol{x}}^-) = \hat{\boldsymbol{q}}_k^-$ $\hat{\boldsymbol{q}}_k^+ = \hat{\boldsymbol{q}}_k^- + \frac{1}{2}\Xi(\hat{\boldsymbol{q}}_k^-)\hat{\boldsymbol{\alpha}}_k^+$, renormalize quaternion $\hat{\boldsymbol{\beta}}_{c_k}^+ = \hat{\boldsymbol{\beta}}_{c_k}^- + \Delta\hat{\boldsymbol{\beta}}_{c_k}^+,\ \hat{\boldsymbol{\beta}}_{d_k}^+ = \hat{\boldsymbol{\beta}}_{d_k}^- + \Delta\hat{\boldsymbol{\beta}}_{d_k}^+$
Propagation	$\hat{\boldsymbol{\omega}}_{c_k}^+ = \tilde{\boldsymbol{\omega}}_{c_k}^+ - \hat{\boldsymbol{\beta}}_k^+,\ \hat{\boldsymbol{\omega}}_{d_k}^+ = \tilde{\boldsymbol{\omega}}_{d_k}^+ - \hat{\boldsymbol{\beta}}_k^+$ $\hat{\boldsymbol{q}}_{k+1} = \bar{\Omega}(\boldsymbol{\omega}_{d_k})\bar{\Gamma}(\boldsymbol{\omega}_{c_k})\hat{\boldsymbol{q}}_k$ $\dot{P}(t) = F(\boldsymbol{x}(t), t)P(t) + P(t)F^T(\boldsymbol{x}(t), t) + G(t)QG^T(t)$

5. Fault-tolerant finite-time controller with full-state feedback

In this section, the fault-tolerant finite-time control of the spacecraft with four reaction wheels (Lee and Leeghim, 2020) are reviewed. The adopted control consists of a feedback control based on the continuous non-singular fast terminal sliding mode method and compensation term based on the finite-time disturbance observer (Lee and Leeghim, 2020). The FTDO is integrated with the NFTSM control to estimate the lumped disturbance, $\hat{\boldsymbol{d}}$ due to external disturbances, actuator faults, parameter uncertainty and actuator saturation. The adopted controller is given as follows and the detail derivations and stability analysis are given in Ref. Lee and Leeghim (2020).

Theorem 5.1. Consider the spacecraft attitude tracking control system (7) and (19) in the presence of actuator faults, inertia uncertainty and external disturbances. All the states in the closed-loop system will converge to a neighborhood of the sliding surface $\boldsymbol{s} = \boldsymbol{0}$ in finite time by applying the following control law:

$$\begin{cases} \boldsymbol{u}_c^{\star} = & \boldsymbol{u}_{eq} + \boldsymbol{u}_{re}, \\ \boldsymbol{u}_{eq} = & (\boldsymbol{\omega}_e + A(\boldsymbol{q})\boldsymbol{\omega}_c)^{\times} J_0(\boldsymbol{\omega}_e + A(\boldsymbol{q})\boldsymbol{\omega}_c) \\ & -J_0(\boldsymbol{\omega}_e^{\times} A(\boldsymbol{q})\boldsymbol{\omega}_c + A(\boldsymbol{q})J_c^{-1}\boldsymbol{\omega}_c^{\times} J_c\boldsymbol{\omega}_c) \\ & -J_0\Lambda_2^{-1}\frac{1}{\gamma_2}\left[I + \Lambda_1\gamma_1 \mathrm{diag}\left(|\boldsymbol{q}_v|^{\gamma_1 - 1}\right)\right] \\ & Q(\boldsymbol{q}^{\star})sig^{2-\gamma_2}(\boldsymbol{\omega}_e) - J_0\boldsymbol{z}_1, \\ \boldsymbol{u}_{re} = & -J_0(k_1\boldsymbol{s} + k_2 sig^{\rho}(\boldsymbol{s})), \end{cases} \tag{47}$$

where a novel non-singular fast terminal sliding mode surface without any constraint and unwinding problem, the sliding surface is defined to achieve attitude tracking in finite time, which is designed as follows:

$$\boldsymbol{s} = \boldsymbol{q}_v^{\star} + \Lambda_1 sig^{\gamma_1}\left(\boldsymbol{q}_v^{\star}\right) + \Lambda_2 sig^{\gamma_2}(\boldsymbol{\omega}_e), \tag{48}$$

in which $\boldsymbol{q}_v^{\star} = \text{sign}(q_4(0))\boldsymbol{q}_v, q_4(0)$ is the initial condition of q_4, and the involved matrices are represented by

$$\Lambda_1 = \text{diag}(\lambda_{11}, \lambda_{12}, \lambda_{13}),\ \Lambda_2 = \text{diag}(\lambda_{21}, \lambda_{22}, \lambda_{23}),$$

with $\lambda_{1i} > 0, \lambda_{2i} > 0, \gamma_{1i} > \gamma_{2i}, 1 < \gamma_{2i} < 2$ for every $i = 1, 2, 3$. The discontinuous function $\text{sign}(q_4(0))$ is defined as

$$\text{sign}(q_4(0)) = \begin{cases} 1, \text{ if}(q_4(0)) > 0 \\ -1, \text{ if}(q_4(0)) < 0. \end{cases} \tag{49}$$

A continuous fast-terminal sliding mode-type reaching law defined in Yu et al. (2005) is empolyed as

$$\dot{\boldsymbol{s}} = -k_1\boldsymbol{s} - k_2 sig^{\rho}(\boldsymbol{s}), \tag{50}$$

where $k_1 = \text{diag}(k_{11}, k_{12}, k_{13}), k_2 = \text{diag}(k_{21}, k_{22}, k_{23}), k_{1i}, k_{2i} > 0, 0 < \rho < 1$. The tracking errors $\boldsymbol{q}_v$ and $\boldsymbol{\omega}_e$ converge to zero with $q_4 = \pm 1$ in finite time.

The notation $\boldsymbol{u}_c^{\star}$ represents the torque design by the baseline controller where the FTDO and NFTSMC are integrated; $\boldsymbol{u}_{cc}$ denotes the command signal to each individual actuator from the control allocation (CA) scheme; $\text{sat}(\boldsymbol{u}_{cc})$ represent the constrained command signal to each individual actuator; $\boldsymbol{u}_{actual}$ represents the actual torque actuator effect on the spacecraft; and $\boldsymbol{\tau}_{actual}$ represents actual torque acting on the spacecraft for attitude maneuvers by the chosen actuator configuration described by D matrix. Thus, the actual torque actuator effect on the spacecraft and the actual torque acting on the spacecraft for attitude maneuvers are described by

$$\boldsymbol{u}_{actual} = ((I - E)\text{sat}(\boldsymbol{u}_{cc}) + E\overline{\boldsymbol{u}}), \tag{51}$$

$$\boldsymbol{\tau}_{actual} = D((I - E)\text{sat}(\boldsymbol{u}_{cc}) + E\overline{\boldsymbol{u}}). \tag{52}$$

However, if there is no actuator fault, the actual torque acting on the spacecraft for attitude maneuvers is described by

$$\boldsymbol{\tau}_{actual} = D\text{sat}(\boldsymbol{u}_{cc}). \tag{53}$$

Assumption 1. The total uncertainty vector $\boldsymbol{d} \in C^2$ which is two times continuously differentiable.

$$|\ddot{d}_i| < \ell_i,\ 1, 2, 3, \tag{54}$$

where ℓ_i is the positive components of $\boldsymbol{\ell} = [\ell_1\ell_2\ell_3]^T$.

By the following 2nd-order differentiator (Pukdeboon and Siricharuanun, 2014; Levant, 2000; Shtessel et al., 2008) with Assumption 1, the lumped disturbance $\boldsymbol{d}$ (19) can be estimated exactly in finite time. Consider the relative attitude dynamics (19) where $\boldsymbol{f}$ is sufficiently smooth functions, the second-order differentiator proposed for the estimate of lumped disturbance $\boldsymbol{d}$ (Lee and Leeghim, 2020) is

$$\begin{cases} \dot{\boldsymbol{z}}_0 = \boldsymbol{f} + J_0^{-1}\boldsymbol{u}_c^{\star} + \boldsymbol{v}_0, \\ v_{0i} = -\lambda_{0i}\left(\ell_i^{2/3}|z_{0i} - \dot{e}_i|^{2/3}\right)\text{sign}(z_{0i} - \omega_{ei}) + z_{1i}, \\ \dot{\boldsymbol{z}}_1 = \boldsymbol{v}_1, \\ \dot{\boldsymbol{v}}_1 = -\lambda_1\left(\ell_i^{1/2}|z_{1i} - v_{0i}|\right) + z_{2i}, \\ \dot{\boldsymbol{z}}_2 = -\lambda_2(\ell)\text{sign}(\boldsymbol{z}_2 - \boldsymbol{v}_1), \end{cases} \tag{55}$$

where $i = 1, 2, 3$ and $\lambda_0, \lambda_1, \lambda_2$ are the observer coefficients, the gain ℓ_i is chosen such that $\ell_i \geqslant |d_i^n|$, where d_i^n denotes $\frac{d^n d_i}{dt^n}$, and $\boldsymbol{z}_3, \boldsymbol{z}_1$ and $\boldsymbol{z}_2$ are the estimates of $\boldsymbol{\omega}_e, J_0^{-1}\boldsymbol{d}$ and $J_0^{-1}\dot{\boldsymbol{d}}$, respectively. Define the estimation error of the disturbance observer as $\boldsymbol{e}_0 = \boldsymbol{z}_0 - \boldsymbol{\omega}_e, \boldsymbol{e}_1 = \boldsymbol{z}_1 - J_0^{-1}\boldsymbol{d}$ and $\boldsymbol{e}_2 = \boldsymbol{z}_2 - J_0^{-1}\dot{\boldsymbol{d}}$. The FTDO's error system becomes

$$\begin{cases} \dot{e}_{0i} = -\lambda_0\left(\ell_i^{2/3}|e_{0i}|^{2/3}\right)\text{sign}(e_{0i}) + e_{1i}, \\ \dot{e}_{1i} = -\lambda_1\left(\ell_i^{1/2}\text{sign}\left(|e_{1i} - \dot{e_{0i}}|^{1/2}\right)\text{sign}(e_{1i} - \dot{e_{0i}}) + e_{2i}, \dot{e}_{2i} \right.\\ \quad = -\lambda_2(\ell_i\text{sign}(e_{2i} - \dot{e}_{1i}) - \ddot{d}_i, \end{cases} \tag{56}$$

Based on the concepts in Levant (2000), (56) is globally finite-time stable. Hence, there exists a fixed constant T such that $\ell_i = 0 (i = 1, 2, 3)$ for $t \geqslant T$. It is known that if the gain ℓ_i is chosen such that $\ell_i \geqslant |d_i^m|$, all the internal signals of FTDOB are bounded and after a finite-time T_i, the error signals $\boldsymbol{e}_0, \boldsymbol{e}_1, \boldsymbol{e}_2$ converge to zero, that is, the disturbance d_i and its derivatives are estimated in finite time. That is $\boldsymbol{z}_0 = \hat{\boldsymbol{\omega}}, \boldsymbol{z}_1 = J_0^{-1}\hat{\boldsymbol{d}}$, and $\boldsymbol{z}_2 = J_0^{-1}\hat{\dot{\boldsymbol{d}}}$. Considering the second-order system (55), there exists a range of gains $\lambda_0, \lambda_1, \lambda_2$ and ℓ_i such that the variables $\boldsymbol{e}_0, \boldsymbol{e}_1, \boldsymbol{e}_2$ can converge to zero in finite time. The detailed proof and gains selection can be found in Levant (2000).

The combined control $\boldsymbol{u}_c^{\star}$ is converted to the command signal for each individual actuator $\boldsymbol{u}_{cc}$ using online pseudo inverse control allocation (CA) scheme. The CA algorithm with more than three actuators for three-axis stabilization/-tracking (Hu et al., 2018) can be derived using a least-square method, that is

$$\min_n \|\boldsymbol{u}_{cc}\|, \text{subject to } D\boldsymbol{u}_{cc} = \boldsymbol{u}_c^{\star}. \tag{57}$$

which is equivalent to the well known pseudo inverse solution $\boldsymbol{u}_{cc} = D^T(DD^T)^{-1}\boldsymbol{u}_c^{\star}$. Next, the command signal for each individual actuator $\boldsymbol{u}_{cc}$ is further specified with explicit consideration of actuator constraint to deal with input saturation problem. The saturation function is defined as follows:

$$\text{sat}(\boldsymbol{u}_{cc}) = \Pi(\boldsymbol{u}_{cc}) \cdot \boldsymbol{u}_{cc}, \tag{58}$$

$$\text{sat}(u_{cci}) = \begin{cases} u_{cci}, & \text{if } |u_{cci}| \leqslant u_m \\ u_m\text{sign}(u_{cci}), & \text{otherwise} \end{cases}, \quad i = 1, 2, \ldots m. \tag{59}$$

where $[u_{cc1}, u_{cc2}, \ldots, u_{ccm}]$ and $u_m > 0$ is the maximum torque that each individual actuator can generate.

$\Pi(\boldsymbol{u}_{cc}) = \text{diag}[\Pi(u_{cc1}), \Pi(u_{cc2}), \ldots, \Pi(u_{ccm})]$, and

$$\Pi_i(u_{cci}) = \begin{cases} 1, & \text{if } |u_{cci}| \leqslant u_m \\ \frac{u_m}{u_{cci}}\text{sign}(u_{cci}), & \text{otherwise} \end{cases}, \quad i = 1, 2, \ldots m. \tag{60}$$

The coefficient $\Pi_i(u_{cci})$ represents an indicator for saturation degree of the i^{th} entry of the control vector, and it satisfies the condition $0 < \Pi_i(u_{cci}) \leqslant 1$. From (17) and (52), the relative attitude dynamics under control input constraints can be described by

$$\begin{aligned} J_d\dot{\boldsymbol{\omega}} = & -(\boldsymbol{\omega}_e + A(\boldsymbol{q})\omega_c)^{\times}J_d(\boldsymbol{\omega}_e + A(\boldsymbol{q})\boldsymbol{\omega}_c) \\ & + J_d\left(\boldsymbol{\omega}_e^{\times}A(\boldsymbol{q})\boldsymbol{\omega}_c + A(\boldsymbol{q})J_c^{-1}\boldsymbol{\omega}_c^{\times}J_c\boldsymbol{\omega}_c\right) \\ & + D(I - E)\text{sat}(\boldsymbol{u}_{cc}) + DE\bar{\boldsymbol{u}} + \boldsymbol{d}_0. \end{aligned} \tag{61}$$

This equation is the governing equation for the relative attitude dynamics between two spacecraft under actuator faults, actuator saturation and unknown external disturbances.

The adopted control (47) was implemented using full state knowledge in Ref. Lee and Leeghim (2020). However, it is important to note that all states must be observed in order to implement the adopted controller in real time. Unfortunately, this is rarely the case in practice. To resolve this problem, the proposed MEKF filter in Table 2 is combined with the adopted control to provide state estimates for the unmeasured states. The block diagram of the attitude estimation and tracking control systems is illustrated in Fig. 2. The estimated relative quaternion, $\hat{\boldsymbol{q}}$ and biases $\hat{\boldsymbol{\beta}}_c, \hat{\boldsymbol{\beta}}_d$ of the chief and deputy spacecraft in the proposed MEKF are used to compute the relative angular velocity $\hat{\boldsymbol{\omega}}$. The estimated $\hat{\boldsymbol{q}}$ and computed $\hat{\boldsymbol{\omega}}$ are incorporated to the FTDO and NFTSM to compute the estimated lumped disturbance $\hat{\boldsymbol{d}}$ and the control $\boldsymbol{u}_c^{\star 0}$, respectively. Thus, the composite attitude control law (47) combined the estimated attitude estimation system is given by

$$\begin{cases} \boldsymbol{u}_c^{\star} = & \boldsymbol{u}_{eq} + \boldsymbol{u}_{re}, \\ \boldsymbol{u}_{eq} = & (\hat{\boldsymbol{\omega}}_e + A(\hat{\boldsymbol{q}})\boldsymbol{\omega}_{ec})^{\times}J_0(\hat{\boldsymbol{\omega}} + A(\hat{\boldsymbol{q}})\boldsymbol{\omega}_c) \\ & -J_0\left(\hat{\boldsymbol{\omega}}_e{}^{\times}A(\hat{\boldsymbol{q}})\boldsymbol{\omega}_c + A(\hat{\boldsymbol{q}})J_c^{-1}\boldsymbol{\omega}_c^{\times}J_c\boldsymbol{\omega}_c\right) \\ & -J_0\Lambda_2^{-1}\frac{1}{\gamma_2}\left[I + \Lambda_1\gamma_1\text{diag}\left(|\hat{\boldsymbol{q}}_v|^{\gamma_1 - 1}\right)\right] \\ & Q(\hat{\boldsymbol{q}}^{\star})sig^{2-\gamma_2}(\hat{\boldsymbol{\omega}}_e) - J_0\boldsymbol{z}_1, \\ \boldsymbol{u}_{re} = & -J_0(k_1\hat{\boldsymbol{s}} + k_2 sig^{\rho}(\hat{\boldsymbol{s}})), \end{cases} \tag{62}$$

where

$$\hat{\boldsymbol{s}} = \hat{\boldsymbol{q}}_v^{\star} + \Lambda_1 sig^{\gamma_1}\left(\hat{\boldsymbol{q}}_v^{\star}\right) + \Lambda_2 sig^{\gamma_2}(\hat{\boldsymbol{\omega}}_e). \tag{63}$$

Thus, the attitude estimation system using the camera and IMU sensors is integrated into the control system with four reaction wheels. The combined attitude control and estimation system expressed by (62) are used to perform attitude tracking maneuvers with a full-state feedback during close-proximity operations.

6. Simulation results

To demonstrate the effectiveness of the proposed ADCS, numerical simulation results are applied for a rigid spacecraft with four reaction wheels as the deputy spacecraft governed by (7) and (19) in conjunction with the adaptive sliding mode control (Zhu et al., 2011), the NFTSMC combining with the FTDO (47), and the proposed control ADCS (62). The Landsat-8 is adopted as a chief spacecraft while Scout Inc.'s Oversat, which will be lunched in 2023, is adopted as a deputy spacecraft to verify the capability of the proposed ADCS system during close-proximity operations. The chief and deputy spacecraft is assumed to have communication so that the chief can provide the attitude states to the deputy during close-proximity operations. The deputy spacecraft will be tested to show both precise relative attitude estimation and control tracking performance from the large inititial attitude error. The four reaction wheels of the deputy spacecraft are mounted in a

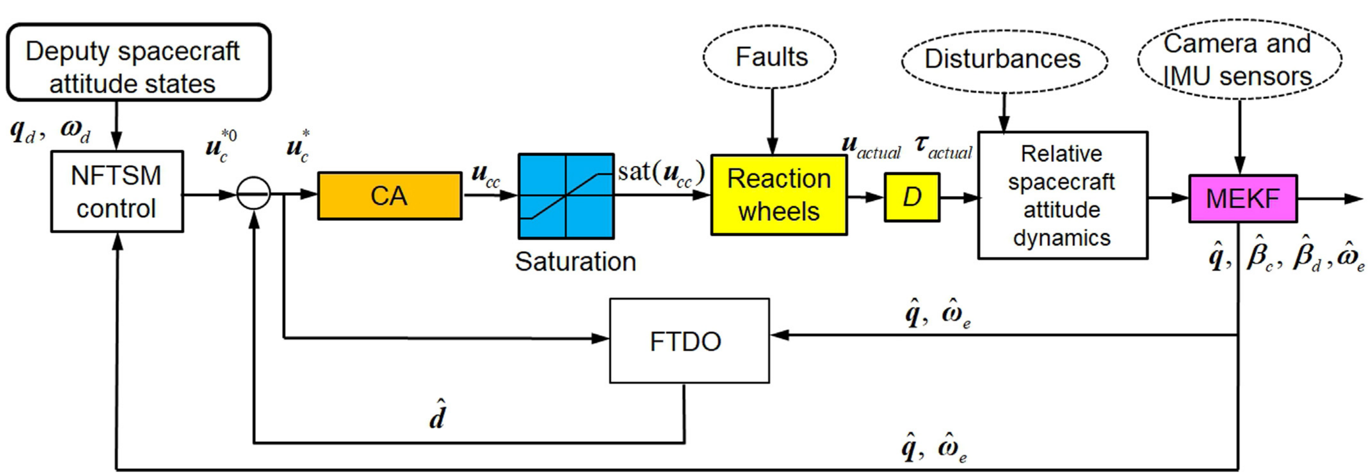

Fig. 2. Block diagram of the attitude estimation/determination and tracking control systems.

tetrahedron configuration, as illustrated in Fig. 3. The advantage of this tetrahedron configuration is that the wheel assembly can provide twice as much of maximum torque on an axis that a single wheel can provide (Kok, 2012). The tetrahedron configuration matrix D is defined as follows (Xiao and Hu, 2013):

$$D = \begin{bmatrix} \sqrt{1/3} & \sqrt{1/3} & -\sqrt{1/3} & -\sqrt{1/3} \\ \sqrt{2/3} & -\sqrt{2/3} & 0 & 0 \\ 0 & 0 & -\sqrt{2/3} & \sqrt{2/3} \end{bmatrix}.$$

To compare the attitude tracking control performances of the ADCS system in Fig. 2 with those of other controllers, the ASMC (Zhu et al., 2011), the NFTSMC (Lee and Leeghim, 2020), and the FTDO-based NFTSMC without anti-unwinding capability (Lee and Leeghim, 2020) are also simulated combining with the proposed attitude estimation system under the same simulation condition. The controller parameters of the chosen controllers listed in Table 3. The inertia matrix of the chief spacecraft, J_c and the inertia matrix of the deputy spacecraft, J_d are specified, respectively, while the inertia uncertainty of the deputy spacecraft is 20 percent, $\Delta J_d = 0.2 J_d$.

$$J_c = \begin{bmatrix} 420.8 & 0 & 0 \\ 0 & 410 & 0 \\ 0 & 0 & 690 \end{bmatrix} \quad \mathrm{kg \cdot m^2},$$

$$J_d = \begin{bmatrix} 20 & 1.2 & 0.9 \\ 1.2 & 17 & 1.4 \\ 0.9 & 1.4 & 15 \end{bmatrix} \quad \mathrm{kg \cdot m^2}.$$

The maximum output torque of each reaction wheel is $u_m = 0.3$ N·m. The external disturbance $\boldsymbol{d}_0(t)$ is taken to account and chosen as

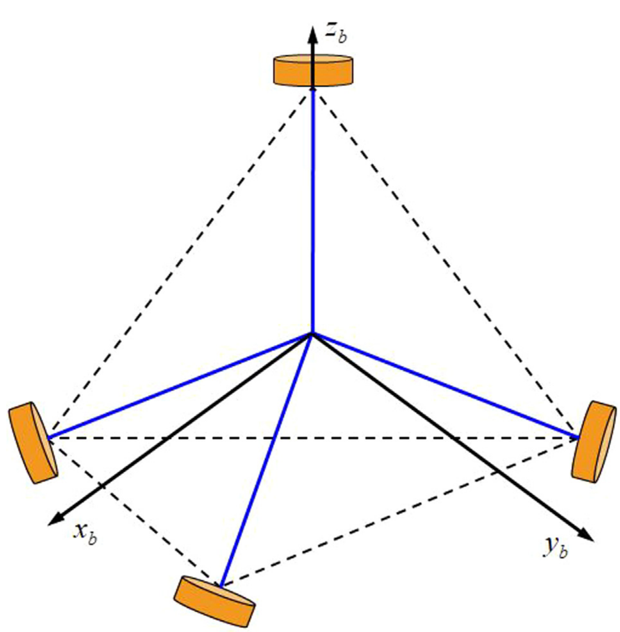

Fig. 3. Tetrahedron configuration of four reaction wheels in the spacecraft body-fixed frame (x_b, y_b, z_b).

$$\boldsymbol{d}_0 = 5 \times 10^{-2} \times \begin{bmatrix} 1 + \sin(\pi t/125) + \sin(\pi t/200) \\ 1 - \sin(\pi t/125) - \sin(\pi t/200) \\ 1 + \cos(\pi t/125) + \cos(\pi t/200) \end{bmatrix} \quad \mathrm{N \cdot m}.$$

To evaluate the control performances under severe actuator faults, the following fault models are used.

$$\begin{aligned} &E_1(t) = \begin{cases} 1, & \text{if} 30 \leqslant t \leqslant 40 \\ 0.6, & \text{ifotherwise} \end{cases}, \\ &E_2(t) = \begin{cases} 1, & \text{if} 30 \leqslant t \leqslant 40 \\ 0.3, & \text{ifotherwise} \end{cases}, \\ &E_3(t) = 0, \qquad E_4(t) = \begin{cases} 1, & \text{if} 30 \leqslant t \leqslant 40 \\ 0.3, & \text{ifotherwise} \end{cases}, \\ &\bar{u}_1(t) = \bar{u}_3(t) = 0, \bar{u}_2(t) = \bar{u}_4(t) = \begin{cases} 0.1, & \text{if} \leqslant 30 \\ 0, & \text{ifotherwise.} \end{cases} \end{aligned} \tag{64}$$

A summary of numerical values of the same simulation parameters for four different controllers and the optical vision (camear sensor) model for determining resolution and measurement uncertainty at indeterminate distances based on normalized resolution is given in Table 4. To demonstrate the ability of the ADCS system in Fig. 2 against unwinding problem, the initial condition of the system state is chosen by $\boldsymbol{q}(0) = [0.3 - 0.2 - 0.3 - 0.8832]^T$ where the sign of the scalar part of $\boldsymbol{q}(0)$, $(q_4(0) < 0)$ is negative and the spacecraft is to rotate an angle $\vartheta = 2\cos^{-1}(0.8832) = 304.06^\circ$ if $[0001]^T$ is the only stable equilibrium. However, rotation for an angle $\vartheta = 2\cos^{-1}(-0.8832) = 360^\circ - 304.07^\circ = 55.93^\circ$ can ensure an unwinding-free attitude tracking if $[000-1]^T$ is considered for a stable equilibrium.

Numerical simulations are performed for 300 s by 10 Hz step size while momentum changes occur for attitude synchronization using four different controllers under the same simulation condition. The initial condition of q_4 is -0.8832, so the closest equilibrium point is $[000-1]^T$. All simulations are performed under the same actuator faults. Fig. 4 presents the additive and multiplicative faults in the reaction wheels of the spacecraft during attitude maneuvers in close-proximity operations using the fault model (64). Some reaction wheels lose partial power and have stuck faults.

6.1. Relative attitude estimation under the actuator faults

In this relative attitude estimation, errors of −50, 60, and 150 deg for each axis of the deputy spacecraft, respectively, are added into the initial condition attitude estimate, with initial bias estimates set to zero. The initial covariance P_0^+ is diagonal with attitude error elements set to $P_{att} = (60\,\mathrm{deg})^2$ and bias error elements set to $P_{bias} = (0.2\,\mathrm{deg/h})^2$. The measurement error covariance sets to $R_k = (0.0337 \times \pi/180)^2 I_3 = (327.58\mathrm{arcsec}) I_3$. The

Table 3
Controller parameters.

Control scheme	Control gains
ASMC (Zhu et al., 2011)	$\tau = 0.5I, \sigma = 0.001I, k = 1, \beta = 30, p_3 = 0.1, \hat{k}_3(0) = 040, \hat{\gamma}(0) = 0.0015$
NFTSMC (Lee and Leeghim, 2020)	$\Lambda_1 = I, \Lambda_2 = 3I, k_1 = k2 = 2I, \gamma_1 = 2.1, \gamma_2 = 1.2$
FTDO-based the NFTSMC (Lee and Leeghim, 2020)	$\Lambda_1 = I, \Lambda_2 = 3I, k_1 = k2 = 2I, \gamma_1 = 2.1, \gamma_2 = 1.2$
Composite control (Lee and Leeghim, 2020)	$\ell = [0.0060.0060.006]^T$

Table 4
Attitude simulation parameters.

Simulation paramters	Values
Initial gyro biases	$\boldsymbol{\beta}_c = [0.10.10.1]$ deg/h
	$\boldsymbol{\beta}_d = [0.10.10.1]$ deg/h
Gyro noises	$\sigma_{cu} = \sigma_{du} = \sqrt{10} \times 10^{-10}$ rad/s$^{3/2}$
	$\sigma_{cv} = \sigma_{dv} = \sqrt{10} \times 10^{-5}$ rad/s$^{1/2}$
Initial angular velocities	$\boldsymbol{\omega}_c = 10^{-3} \times [0.30 - 0.600.21]^T$ rad/s
	$\boldsymbol{\omega}_d = [0.0999 - 0.10070.0998]^T$ rad/s
	$\boldsymbol{\omega}_e = [0.1 - 0.10.1]^T$ rad/s
Initial quaternions	$\boldsymbol{q}_c = [0.6736 - 0.0534 - 0.73520.0534]^T$
	$\boldsymbol{q}_d = [-0.70990.01800.5146 - 0.4805]^T$
	$\boldsymbol{q}_e = [0.3000 - 0.2000 - 0.3000 - 0.8832]^T$
Initial observer state	$z_1 = z_2 = z_3 = [000]^T$
Focal length, f_l	0.25 m
Distance between the focal plane and feature of interest, D,	10 m
pixel pitch, p	4.8×10^{-6}
Optical wavelength of the sensor, λ	55×10^{-6}m
σ_q	0.0017 deg

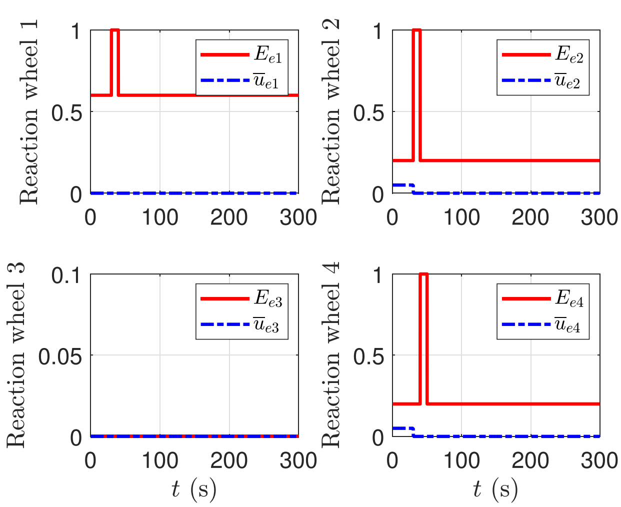

Fig. 4. Applied actuator faults.

attitude estimation results are obtained under the actuator faults. The attitude control and estimation simulations are performed with the values in Table 4 including the imaging model in Section 3.2. Fig. 5(a) and (b) show the chief and deputy bias estimates, which are well estimated by the MEKF after 200 s. Fig. 5(c) shows the relative attitude estimation errors and 3σ bounds derived from the MEKF error covariance matrix. All errors remain within their respective bounds, which means that the MEKF works properly. From the large initial attitude error, the relative attitude estimation errors go down quickly and are within 0.05 deg. The convergence of the relative attitude estimation errors can be obviously observed in Fig. 5(d) where the norm of the relative attitude estimation errors converge to within 1 s and lower than 0.01 deg after 1 s. This indicates that the MEKF promptly achieves precise attitude estimation. Fig. 5(d) shows the relative angular velocity estimates using (35b). The norm of relative angular velocity errors converge to within 2×10^{-5} rad/s after 1 s. Thus, the MEKF using a camera sensor and two gyros shows that it can provide high-precision relative attitude estimation result whose estimation error is within 0.1 deg even from an initial large attitude error within 1 s. Table 5 shows the RMS (root mean square) errors of the attitude estimation under actuator faults and large intial attitude errors for 30 s.

6.2. Attitude tracking results under the actuator faults

In this section, the attitude tracking results of the ADCS system are compared with the controllers combined with the proposed EKF system. Fig. 6 shows the sliding surface (63) approach zero after 50 s, which indicates that the adopted controller combined with the MEKF drives the attitude states to the sliding surface $\boldsymbol{s} = \boldsymbol{0}$. Fig. 7 shows

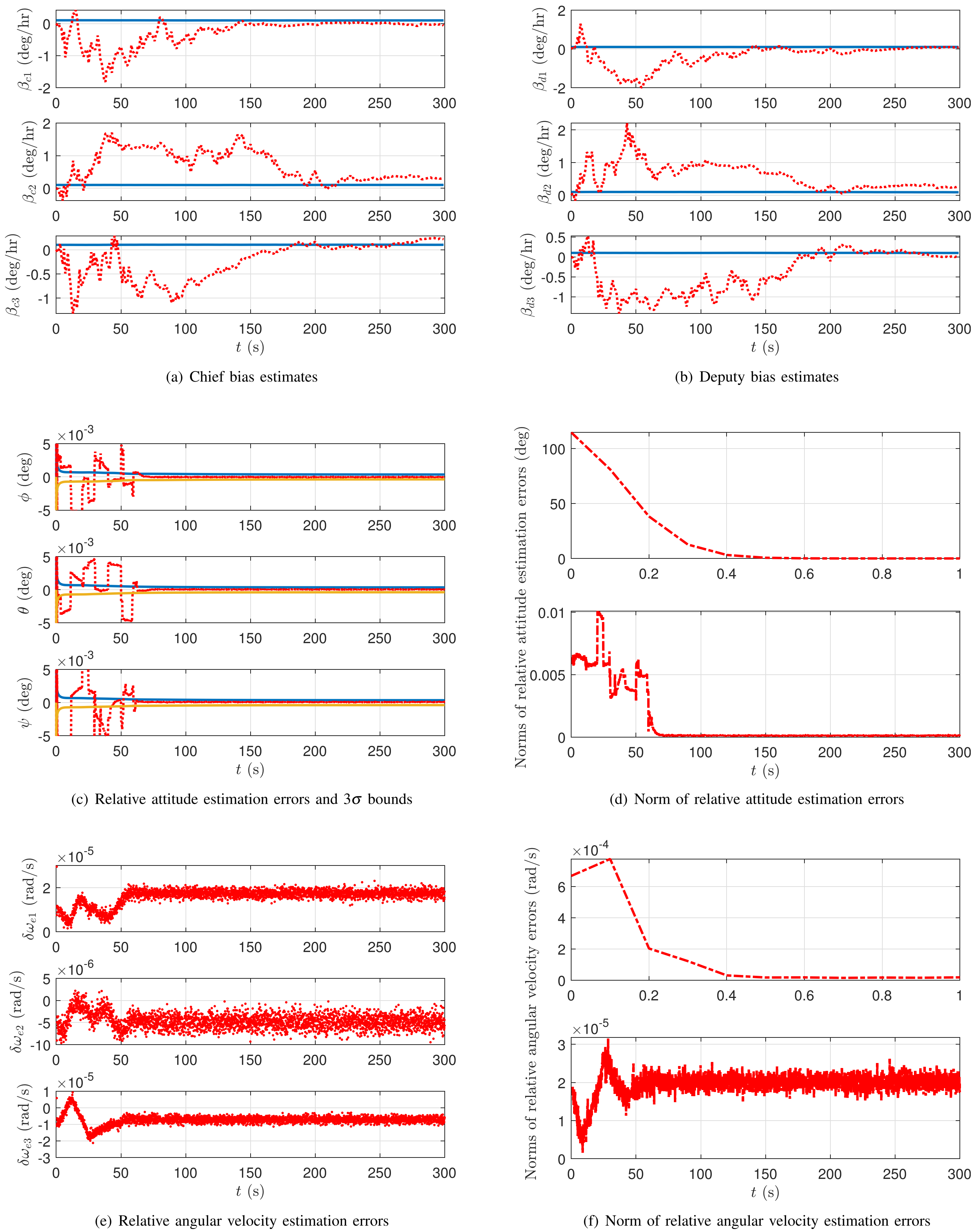

(a) Chief bias estimates

(b) Deputy bias estimates

(c) Relative attitude estimation errors and 3σ bounds

(d) Norm of relative attitude estimation errors

(e) Relative angular velocity estimation errors

(f) Norm of relative angular velocity estimation errors

Fig. 5. Gyro bias estimates, relative attitude errors and computed relative angular velocity.

Table 5
Root mean square errors for the attitude estimation.

RMS error	Value
Roll (deg)	2.15
Pitch (deg)	0.65
Yaw (deg)	1.44
$\delta\omega_1$ (rad/s)	1.866×10^{-5}
$\delta\omega_2$ (rad/s)	1.693×10^{-5}
$\delta\omega_3$ (rad/s)	1.426×10^{-5}
Obersvation residuals	2.686×10^{-3}

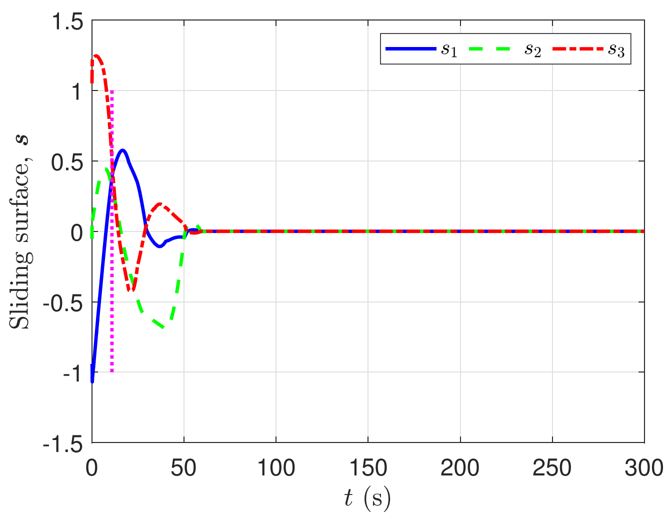

Fig. 6. Sliding surface using the ADCS.

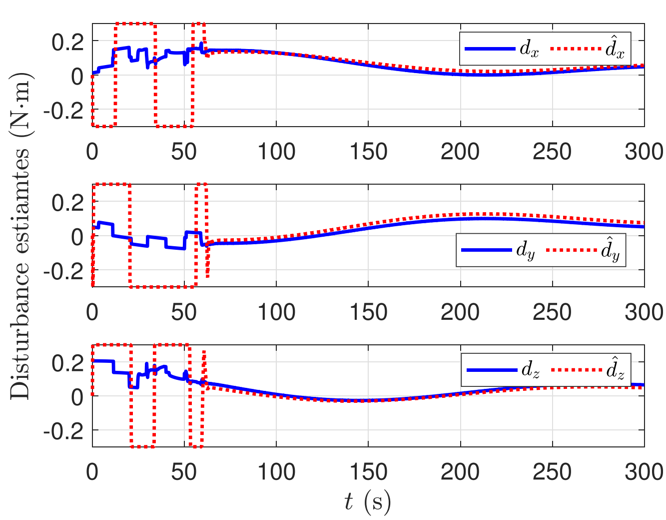

Fig. 7. Lumped disturbance estimates.

the estimate of the lumped disturbance $\hat{\boldsymbol{d}}$ with the actual lumped disturbance $\boldsymbol{d}$. The convergence of $\hat{\boldsymbol{d}}$ to $\boldsymbol{d}$ takes about 60 s with some oscillations due to the actuator faults.

Fig. 8 shows time responses of the attitude tracking results represented by the relative quaternion, $\boldsymbol{q}_e$ and relative angular velocity, $\boldsymbol{\omega}_e$ with four different controllers combined with the proposed EKF under actuator faults, external disturbances and the uncertain inertia matrix. The ASMC (Zhu et al., 2011) and the FTDO-based NFTSMC without anti-winding capability (Lee and Leeghim, 2020) in Fig. 8(a) and (c) show unwinding problem getting to the equilibrium [0001] instead of [000 − 1]. On the other hand, the NFTSMC (Lee and Leeghim, 2020) and the proposed ADCS in Fig. 8(b) and (d) which have anti-unwinding capability show the convergence to the closer equilibrium [000 − 1]. They obviously show faster attitude tracking results than the ASMC (Zhu et al., 2011) and the FTDO-based NFTSMC which does not have anti-winding capability (Lee and Leeghim, 2020). Fig. 9 shows time responses of control command via input saturation, sat($\boldsymbol{u}_{cc}$) under actuator faults, external disturbances and the uncertain inertia matrix. The ASMC (Zhu et al., 2011) and the FTDO incorporated with the NFTSMC without anti-winding capability (Lee and Leeghim, 2020) require higher control responses. To compare the attitude tracking performances of four different methods, the attitude tracking errors and control commands via input saturation are quantified. The performance indices are obtained by numerically integrating the norms of the attitude tracking errors by Euler angle errors using a common simplification given by the small angle approximation (Crassidis and Junkins, 2008), and the norms of control torques over the simulation run, given by

$$J_e = \int_0^{t_f} \|\boldsymbol{e}(t)\| dt, \tag{65}$$

$$J_{u_{actual}} = \int_0^{t_f} \|\boldsymbol{u}_{actual}(t)\| dt, \tag{66}$$

where $\boldsymbol{e}(t)$ denotes the roll, pitch and yaw errors. The performance indices for the attitude control performances of four different methods combined with the MEKF are listed in Table 6. Among them, the proposed ADCS which combines the proposed control (Lee and Leeghim, 2020) and the MEKF shows the smallest J_e, which indicates that its accumulated attitude error is the smallest. The proposed ADCS and the NFTSMC (Lee and Leeghim, 2020) combine with the MEKF show a very similar value in $J_{u_{actual}}$ and smaller values of the ASMC and the FTDO-based NFTSMC (Lee and Leeghim, 2020) combined with the MEKF. It means that they are also efficient in consuming the control torque while the attitude tracking maneuvers are performed.

Figs. 10 and 11 show the norms of attitude tracking errors and energy consumption indices (66) for four different controllers combined with the MEKF under severe actuator fault models using (64) and external disturbance. The proposed ADCS obviously shows the smallest norms of the attitude tracking errors while the energy index by the ADCS shows a little bigger than than that of the NFTSMC (Lee and Leeghim, 2020). It is due to the additional use of control torque requested by the FTDO to cope with the lumped disturbance. It is also due to the fact

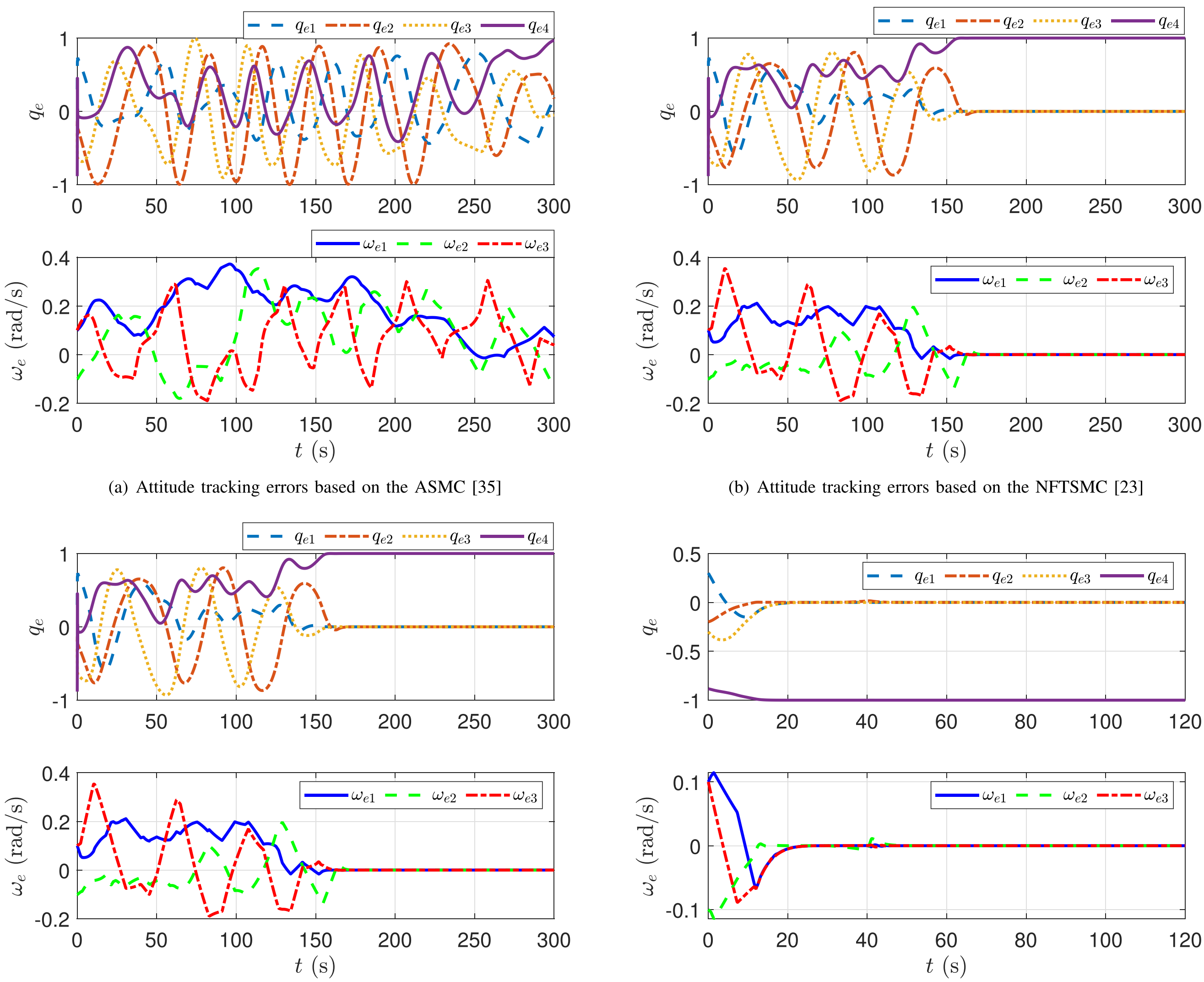

(a) Attitude tracking errors based on the ASMC [35]

(b) Attitude tracking errors based on the NFTSMC [23]

(c) Attitude tracking errors based on the FTDO incorporated with the NFTSMC without anti-unwinding capability [23]

(d) Attitude tracking errors using the proposed ADCS

Fig. 8. Time responses of the attitude tracking results.

that the proposed control in Ref. Lee and Leeghim (2020) has only capability to drive the attitude states into the neighborhood of the surface $\boldsymbol{s} = \boldsymbol{0}$ rather than onto the sliding surface in the presence of actuator faults. It is also obvious to observe the norms of attitude tracking errors by the proposed ADCS in Fig. 10 reduce fastest among them. Note that the norms of attitude tracking errors by the NFTSMC (Lee and Leeghim, 2020) and the proposed ADCS go down quickly within 60 s while actuator faults occur to get to the closer equilibrium $[000-1]^T$ while the ASMC and FTDO-based NFTSMC drive the quaternion states to the further equilibrium state $[0001]^T$ by consuming bigger control power and taking longer tracking time, which results in unwinding problem. Fig. 11 shows the energy indices of the proposed ADCS are obviously smaller compared to those of the ASMC (Zhu et al., 2011) and the FTDO-based NFTSMC without anti-unwinding capability (Lee and Leeghim, 2020). The energy index of the proposed ADCS in Fig. 11 is a little higher than the energy index of the NFTSMC (Lee and Leeghim, 2020) because the FTDO in the proposed ADCS compensates for the actuator faults, external disturbances and inertia uncertainty by commanding higher control power. These simulation results verify that the ADCS show finite-time convergence, fault tolerant and anti-unwinding capabilities, and robustness to external disturbances and inertia uncertainty.

7. Conclusion

A real-time high-precision relative attitude estimation method using a camera sensor and two gyros was developed and combined with a fault-tolerant finite-time attitude tracking control law to develop an ADCS for

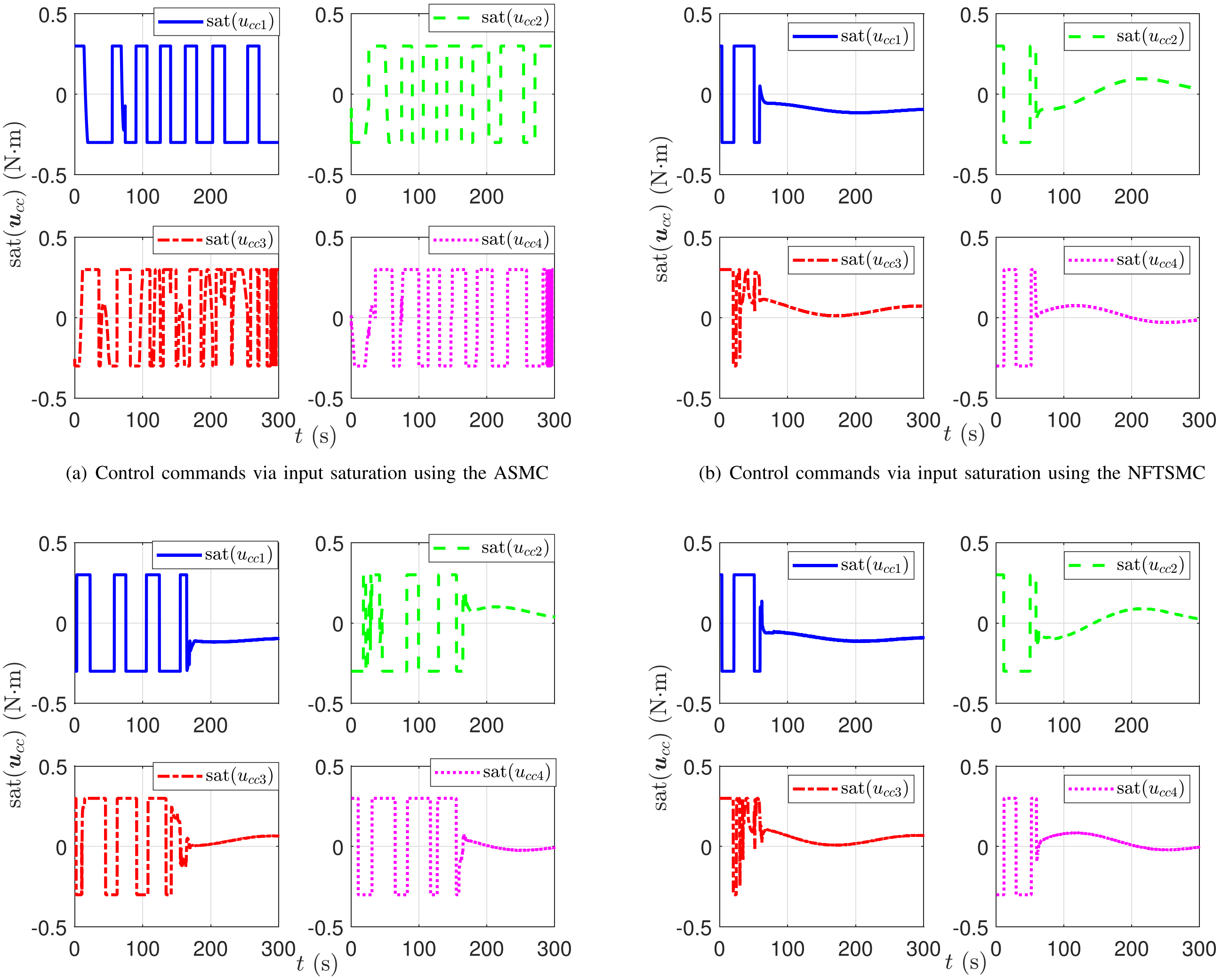

(a) Control commands via input saturation using the ASMC

(b) Control commands via input saturation using the NFTSMC

(c) Control commands via input saturation using the FTDO incorporated with the NFTSMC

(d) Control commands via input saturation using the proposed ADCS

Fig. 9. Time responses of control commands via input saturation, sat($\boldsymbol{u}_{cc}$).

Table 6
Attitude control performances of four different methods combined with the MEKF.

Performance index	Used control method			
	ASMC (Zhu et al., 2011)	NFTSMC (Lee and Leeghim, 2020)	FTDO-based NFTSMC (Lee and Leeghim, 2020)	Proposed control (Lee and Leeghim, 2020)
J_e	2.964×10^4	3.276×10^3	1.422×10^4	3.244×10^3
$J_{u_{actual}}$	99.906	24.266	58.509	24.687

attitude tracking maneuvers during close-proximity operations. The MEKF was adopted to process quaternion measurements without violating a quaternion constraint. The proposed ADCS takes the full-state feedback form combining the FTDO-based NFTSMC and the developed high-precision relative attitude estimation method that provides a full-state knowledge of the estimation to the control law instead of the true state which was used in the the FTDO-based NFTSMC. The proposed ADCS system has finite-time stability and anti-unwinding capability in the presence of external disturbances, inertia uncertainty, and actuator faults. Numerical simulations were performed in conjunction with three other control laws combined with the MEKF in the presence of external disturbances, uncertain inertia parameter, and actuator faults to demonstrate the effectiveness of the proposed attitude estimation and control system. The simulation results show that the relative attitude estimation errors by the MEKF are within

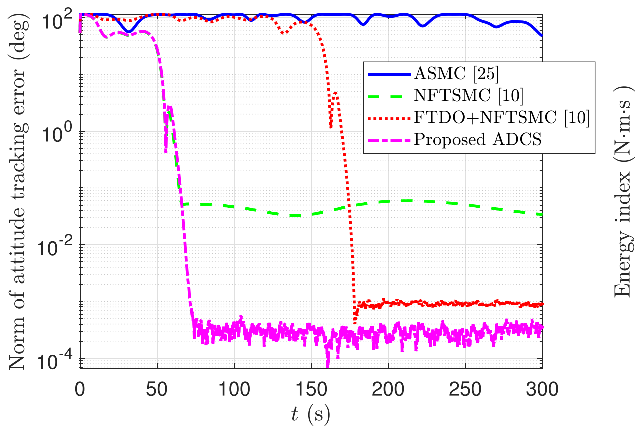

Fig. 10. Norms of attitude tracking errors.

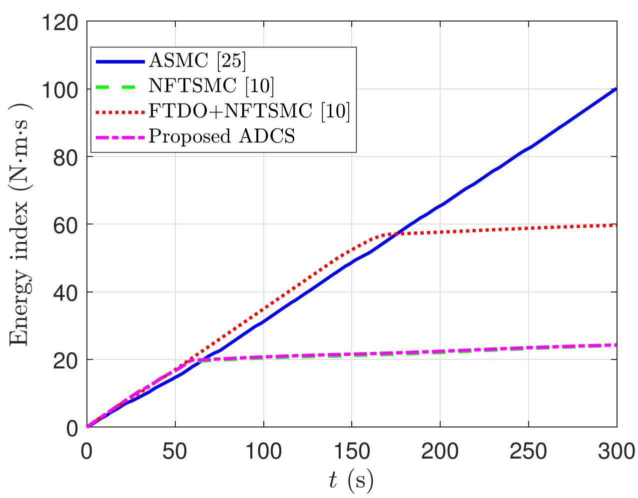

Fig. 11. Energy consumption indices.

0.05 deg after 1 s from the large initial attitude error. The proposed ADCS also shows fault-tolerant, anti-unwinding capability, and precise attitude tracking convergence in finite time while the control momentum is more efficiently saved the conventional control laws. Thus, the effectiveness of the proposed ADCS system was successfully verified with for an attitude tracking control maneuver during close-proximity operations.

Declaration of Competing Interest

The authors declare that they have no known competing financial interests or personal relationships that could have appeared to influence the work reported in this paper.

Acknowledgments

The work was supported in part by the NASA SBIR contract 22-1-S16.03-1719.

Appendix A. The probability spread function of a received discernible (unit) signal within the magnitude threshold for pixel-level binning of observed objects is assumed to be normal. The functional resolution is calculated based on the full-width half magnitude (FWHM) wavelength of the sensor. By definition of a normal probability curve, the integrated signal with greater than 50 % amplitude is roughly invariant and corresponds with $2\sigma_z\sqrt{2\log(2)} = 2.35\sigma_z$. σ_z represents the standard deviation of any arbitrary normal distribution function. This constitutes approximately 75 % of the full signal area, or a probability space defined by a Z-score of 0.68. The team conducted empirical testing of a variety of vision algorithms using contrast detection and neural network-based feature detection and inference as baselines which yielded a tuned Z-score of reference for the imaging application to be 0.66, which corresponds with an aggregate probability space for a normal curve of 0.7454.

References

Abdelrahman, M., Park, S.-Y., 2011. Sigma-point kalman filtering for spacecraft attitude and rate estimation using magnetometer measurements. IEEE Trans. Aerosp. Electron. Syst. 47 (2), 1401–1415.

Cao, T., Gong, H., Cheng, P., Xue, Y., 2022. A novel learning observer-based fault-tolerant attitude control for rigid spacecraft. Aerosp. Sci. Technol. 128.

Crassidis, J.L., 2005. Sigma-point kalman filtering for integrated gps and inertial navigation. In: Collection of Technical Papers - AIAA Guidance, Navigation, and Control Conference. San Francisco, CA, United States, pp. 1981–2004.

Crassidis, J.L., Junkins, J.L., 2008. Optimal Estimation of Dynamic Systems, 2nd ed. CRC Press, Boca Raton, Florida, USA, pp. 452–454.

Du, H., Li, S., Qian, C., 2011. Finite-time attitude tracking control of spacecraft with application to attitude synchronization. IEEE Trans. Automat. Contr. 56 (11), 2711–2717.

Farrenkopf, R., 1978. Analytic steady-state accuracy solutions for two common spacecraft attitude estimators. J. Guid. Control Dyn. 1 (4), 282–284.

Hu, Q., Huo, X., Xiao, B., 2013. Reaction wheel fault tolerant control for spacecraft attitude stabilization with finite-time convergence. Int. J. Robust Nonlinear Control 23 (15), 1737–1752.

Hu, Q., Tan, X., Akella, M.R., 2017. Observer-based attitude control for satellite under actuator fault. J. Guid. Control Dyn. 40 (10), 2524–2537.

Hu, Q., Shao, X., Chen, W.-H., 2018. Robust fault-tolerant tracking control for spacecraft proximity operations using time-varying sliding mode. IEEE Trans. Aerosp. Electron. Syst. 54 (1), 2–17.

Jiang, B., Hu, Q., Friswell, M.I., 2016. Fixed-time attitude control for rigid spacecraft with actuator saturation and faults. IEEE Trans. Control Syst. Technol. 24 (5), 1892–1898.

Kim, S.-G., Crassidis, J.L., Cheng, Y., Fosbury, A.M., Junkins, J.L., 2007. Kalman filtering for relative spacecraft attitude and position estimation. J. Guid. Control Dyn. 30 (1), 133–143.

Kok, I., 2012. Comparison and analysis of attitude control systems of a satellite using reaction wheel actuators Master's Thesis. Lulea University of Technology.

Lan, Q., Qian, C., Li, S., 2017. Finite-time disturbance observer design and attitude tracking control of a rigid spacecraft. J. Dyn. Syst. Meas. Contr. 139 (6), 061 010-1–061 010-8.

Lee, D., 2017. Nonlinear disturbance observer-based robust control of attitude tracking of rigid spacecraft. Nonlinear Dyn. 88 (2), 1317–1328.

Lee, D., 2021. Finite-time fault-tolerant control for attitude tracking of rigid spacecraft using new intermediate quaternion. IEEE Trans. Aerosp. Electron. Syst. 57 (1), 540–553.

Lee, D., Leeghim, H., 2020. Reaction wheel fault-tolerant finite-time control for spacecraft attitude tracking without unwinding. Int. J. Robust Nonlinear Control 30 (9), 3672–3691.

Lefferts, E., Markley, F., Shuster, M., 1982. Kalman filtering for spacecraft attitude estimation. J. Guid. Control Dyn. 5 (5), 417–429.

Levant, A., 2000. Higher-order sliding modes, differentiation and output-feedback control. Int. J. Control 76 (9–10), 924–941.

Liebe, C., 1995. Star trackers for attitude determination. IEEE Aerosp. Electron. Syst. Mag. 10 (6), 10–16.

Lu, K., Xia, Y., 2013. Adaptive attitude tracking control for rigid spacecraft with finite-time convergence. Automatica 49 (12), 3591–3599.

Lu, K., Xia, Y., Fu, M., Yu, C., 2016. Adaptive finite-time attitude stabilization for rigid spacecraft with actuator faults and saturation constraints. Int. J. Robust Nonlinear Control 26 (1), 28–46.

Mayo, R.A., 1978. Relative quaternion state transition relation. J. Guid. Control Dyn. 2 (1), 44–48.

Park, T.H., Sharma, S., Amico, S.D., 2019. Towards robust learning-based pose estimation of noncooperative spacecraft. AAS/AIAA Astrodynamics Specialist Conference, vol. 171. AAS, pp. 19–840.

Pukdeboon, C., Siricharuanun, P., 2014. Nonsingular terminal sliding mode based finite-time control for spacecraft attitude tracking. Int. J. Control Autom. Syst. 12 (3), 530–540.

Sajjadi, M., Chahari, M., Vossoughi, G., 2021. Designing nonlinear observer for topography estimation in trolling mode atomic force microscopy. J. Vib. Control 28 (23–24), 10775463211038140.

Schmidt, S.F., 1981. The kalman filter: Its recognition and development for aerospace applications. J. Guid. Control Dyn. 4 (1), 4–7.

Shen, Q., Wang, D., Zhu, S., Poh, E.K., 2015. Inertia-free fault-tolerant spacecraft attitude tracking using control allocation. Automatica 62, 114–121.

Shtessel, Y.B., Fridman, L., Zinober, A., 2008. Higher order sliding modes. Int. J. Robust Nonlinear Control 18, 381–384.

Tewari, A., 2007. Atmospheric and Space Flight Dynamics. Birkhauser Boston.

Tiwari, P.M., Janardhanan, S., un-Nabi, M., 2018. Spacecraft anti-unwinding attitude control using second-order sliding mode. Asian J. Control 20 (1), 455–468.

Wang, X., Abtahi, S.M., Chahari, M., Zhao, T., 2022. An adaptive neuro-fuzzy model for attitude estimation and control of a 3 dof system. Mathematics 10 (6), 976.

Xiao, B., Hu, Q., 2013. Reaction wheel fault compensation and disturbance rejection for spacecraft attitude tracking. J. Guid. Control Dyn. 36 (6), 1565–1575.

Yu, S., Yu, X., Shirinzadeh, B., Mand, Z., 2005. Continuous finite-time control for robotic manipulators with terminal sliding mode. Automatica 41 (11), 1957–1964.

Zhu, Z., Xia, Y., Fu, M., 2011. Adaptive sliding mode control for attitude stabilization with actuator saturation. IEEE Trans. Industr. Electron. 58 (10), 4898–4907.

Zou, A.-M., 2014. Finite-time output feedback attitude tracking control for rigid spacecraft. IEEE Trans. Control Syst. Technol. 22 (1), 338–345.